WSRC-TR-92-543 (U)

685006

KEYWORDS:
New Production Reactor
Loss of Coolant Accident
Stainless Steel Corrosion
Liquid Metal Embrittlement
RETENTION - Permanent

DISSOLUTION OF STAINLESS STEEL BY MOLTEN ALUMINUM AND ALUMINUM ALLOYS — FINAL REPORT (U)

JAMES C. MARRA
SAVANNAH RIVER TECHNOLOGY CENTER
Materials Technology Section

Publication Date: November, 1992

Westinghouse Savannah River Company
Savannah River Site
Aiken, SC 29808

This document was prepared in conjunction with work accomplished under Contract No. DE-AC09-96SR18500 with the U.S. Department of Energy.

DISCLAIMER

WSRC-TR-92-543 (U)

DISSOLUTION OF STAINLESS STEEL BY MOLTEN ALUMINUM AND ALUMINUM ALLOYS — FINAL REPORT (U)

JAMES C. MARRA

Reviewing Official: D. Thomas Rankin

Authorized Derivative Classifier

Date: 11/19/92

Westinghouse Savannah River Company
Savannah River Site
Aiken, SC 29808

SAFETY • RESPONSIBILITY • SECURITY

SRS

SAVANNAH RIVER SITE

THIS PAGE INTENTIONALLY LEFT BLANK

TABLE OF CONTENTS PAGE

LIST OF TABLES **PAGE**

LIST OF FIGURES

LIST OF FIGURES (continued) PAGE

LIST OF FIGURES (Continued) PAGE

LIST OF FIGURES (Continued) **PAGE**

APPROVALS

James C. Marra Date: 11/19/92
James C. Marra, AUTHOR
Materials Compatibility & Joining Technology Group
MATERIALS TECHNOLOGY SECTION

Jerry P. Morin Date: 11/23/92
Jerry P. Morin, CUSTOMER
New Production Reactor Program

Elliot A. Clark Date: 11/19/92
Elliot A. Clark, TECHNICAL REVIEWER
MATERIALS TECHNOLOGY SECTION

D. Thomas Rankin Date: 11/19/92
D. Thomas Rankin, MANAGER
Materials Compatibility & Joining Technology Group
MATERIALS TECHNOLOGY SECTION

Tami L. Capeletti Date: 11/24/92
Tami L. Capeletti, MANAGER
MATERIALS TECHNOLOGY SECTION

THIS PAGE INTENTIONALLY LEFT BLANK

EXECUTIVE SUMMARY

The purpose of this task was to investigate on a laboratory-scale the interactions of molten aluminum with stainless steel under hypothetical severe reactor accident conditions. This experimental effort provided data necessary to assess the susceptibility of the reactor vessel to breaching (general through-wall failure of vessel) in accident scenarios where contact of molten aluminum and stainless steel may occur. This report summarizes the results of the extensive experimental program.

Many variables influenced the dissolution of stainless steel by molten aluminum including: temperature, melt flow rate, steel surface oxide condition, molten alloy composition and solubility of steel in molten aluminum. Increases in melt temperatures dramatically increased the dissolution rates. Dissolution rate also showed a direct dependance on sample rotation rates (i.e. melt flow rate). Although efforts were made to minimize oxide films on the stainless steel, attack primarily originated preferentially where the oxide film was readily broken down. The addition of depleted uranium into the molten Al alloy decreased the dissolution rate. Although widespread variations in dissolution rates occurred from test to test, the rate of attack typically slowed as the concentration of steel increased in the aluminum melts.

The dissolution of stainless steel by molten aluminum is a diffusion controlled process. At the lower test temperatures (700 and 900° C), dissolution occurred by the passage of the steel constituent elements into the melt. In tests at 1100° C, a dual diffusion mechanism likely occurred where the molten Al also diffused into the steel causing rapid attack. The boron additions in borated steel samples (existing as insoluble chromium-boride compounds) passed into the Al melt during dissolution and remained insoluble and generally well-dispersed.

Embrittlement of stainless steel by molten aluminum was not evident in the qualitative liquid metal embrittlement (LME) susceptibility tests performed. A decrease in time to failure, however, was consistently observed for Al coated steel samples in constant load tests. This decrease was likely due to dissolution.

INTRODUCTION

In the unlikely event of a severe reactor accident involving complete loss of coolant, in the proposed Ebasco designed heavy water New Production Reactor (NPR), aluminum-based fuel and target elements could melt resulting in a pool of molten aluminum-uranium and debris contacting the reactor vessel [1]. In this scenario, temperatures of

the melt as high as 1100 - 1200° C have been postulated [1]. The dissolution of stainless steel by molten aluminum is known to occur [2-4]. Dissolution can occur at temperatures as low as the melting temperature of the aluminum. An important aspect of the NPR design philosophy includes the objective to arrest the progression of severe accidents, if possible, prior to the breach of the primary system [1]. It was, therefore, necessary to investigate the interactions of molten aluminum and aluminum alloys with stainless steel under hypothetical accident conditions. The purpose of this investigation was to provide data necessary to assess the susceptibility of the reactor vessel to breaching in accident scenarios where contact of molten aluminum and the reactor vessel are likely. The Materials Technology Section of the Savannah River Technology Center was tasked to examine this interaction by the New Production Reactor Division. This report summarizes the results of the experimental program.

LITERATURE SURVEY

Dissolution

Molten aluminum has been shown to attack stainless steel, certain refractory metals and iron alloys [2-8]. The dissolution of stainless steel by molten aluminum begins by the rapid formation of intermetallic layers at the liquid aluminum-stainless steel surface. The attack on the steel proceeds by the diffusion of the constituent atoms of the steel through the interfacial layers into the aluminum melt with iron being the rate controlling species [2]. This diffusion controlled process was found by Dybkov to be non-selective, that is the major constituent atoms of the steel pass into the aluminum in the same ratios as are present in the steel, in tests performed between 700 - 850° C [2]. The rate of dissolution is, therefore, controlled by the relative solubility of the stainless steel constituent atoms in the aluminum. The rate is observed to decrease as the solubility limit is approached and eventually ceases when the limit is reached [2,8].

A number of factors are expected to influence the nature and rate of attack of stainless steel by molten aluminum. These include: temperature of the melt, exposure time (solubility effects), oxide films on the stainless steel and aluminum, hydrodynamics of the melt and molten alloy composition.

The dissolution of a solid metal into a liquid metal is typically described by an expression of the form [9]:

$$J = k (C - c) \qquad (1)$$

where: J = net rate of dissolution (mass flux) (mol/m^2-s)
k = dissolution rate constant for rate controlling step (m/s)
C = solubility of element in liquid metal (mol/m^3)
c = instantaneous concentration of element in liquid metal (mol/m^3)

Additionally, the dissolution rate constant (k) for solid metals in molten metals typically obeys the Arrhenius relation:

$$k = k_o \exp(-E/RT) \qquad (2)$$

where: k = dissolution rate constant (m/s)
k_o = pre-exponential factor (m/s)
E = activation energy (J/mol)
R = gas constant (J/mol-K)
T = temperature (K)

Equations 1 and 2 show that as the aluminum melt temperature increases, the initial stainless steel dissolution rate increases. Additionally, as the steel concentration in the aluminum melt increases with increased exposure time, the dissolution rate decreases and dissolution eventually ceases when the saturation concentration (C) is reached.

The dissolution of metals in molten aluminum with regard to melt temperature has been studied extensively [2-6,8]. Yeremenko, et al. investigated the interaction of several refractory metals with molten aluminum in the temperature range of 700 - 850° C [6]. In these experiments, the dissolution rate constants (and diffusion coefficients) showed increases with increasing melt temperatures for all the metals tested consistent with an Arrhenius relation. Similar behavior was observed in work by Niinomi, et al. on ferrous alloys exposed to molten aluminum at temperatures from 700 - 800° C [5]. Webb and Pohlman investigated the interaction of Type 316 stainless steel with molten aluminum in the temperature range 705 - 927° C for a potential thermal receiver application [4]. The dissolution data, based on a localized or "pitting" attack argument, showed that the depth and concentration of pits increased exponentially with temperature. A thorough investigation of the interaction of a stainless steel (similar to Type 304) with molten aluminum was performed by Dybkov [2]. Although concentrations of stainless steel increased in the melt with increasing melt temperatures (i.e. increased dissolution), little variation was observed in

dissolution rate constant as calculated using a derived expression from equation 1. As dissolution rate constant is directly related to the diffusion coefficient and inversely related to melt viscosity (see below), Dybkov rationalized that these variables offset one another causing no change in dissolution rate constant. From the above studies, it is clear that an increase in dissolution accompanies an increase in melt temperature. However, these studies did not provide dissolution rate information for higher melt temperatures in-line with hypothesized severe reactor accident conditions.

The effect of stainless steel constituent concentration in the aluminum melt on dissolution was examined by Dybkov [2]. Tests were performed using the same melt with multiple exposed steel samples until dissolution ceased. Steel element concentration vs. time plots revealed a gradual curvature from linearity as the concentration increased and eventually reached saturation. The saturation concentration of Fe in Al coincided with the solubility of iron in aluminum from the binary phase diagram, while the solubilities of Ni and Cr in Al were well below their respective solubilities in aluminum. Further, concentrations of respective elements of the stainless steel in the melt agreed with the chemical analysis of the original steel indicating the non-selective nature of the attack. Unpublished work by Mosley showed similar decreases in dissolution rates with an increase of stainless steel concentration in the melt [8].

The formation of a protective oxide film on austenitic stainless steels leads to enhanced corrosion resistance. Similarly, this protective film should provide resistance to attack from molten aluminum by inhibiting wetting. Dybkov used extreme measures to inhibit oxide film formation on the stainless steel [2]. Steel samples were mechanically ground and polished prior to exposure and a special flux was used to protect the sample and melt from oxidation before and during the testing. These measures resulted in a "general" type of attack on the exposed coupons. Webb and Pohlman assessed the effects of stainless steel surface condition on attack by molten aluminum [4]. "Pitting" type attack was observed for both polished and unpolished specimens in tests conducted in air in a muffle furnace. Additionally, no significant weight loss variations were attributed to the variations in surface condition. Previous work by Marra showed variations in dissolution rates for Type 316L steel samples with various initial surface conditions [10]. Coupons ground immediately prior to immersion in an Al melt heated in air showed consistently higher dissolution rates than as-received and chemically passivated coupons.

The dissolution rate of solids in liquids strongly depends on the degree of agitation of the liquid. Dybkov described a dependence for a rotating disk as defined by Levich [2]. The dissolution rate constant varies with the angular velocity of the rotating sample as follows:

$$k = 0.62D^{2/3}v^{-1/6}w^{1/2} \qquad (3)$$

where: k = dissolution rate constant (m/s)
D = diffusion coefficient (m^2/s)
v = kinematic viscosity (m^2/s)
w = angular velocity (rad/s)

Dybkov, in his work with laminar flow conditions, showed that the dissolution rate constant correlated with the square root of the angular velocity. In an intensive review of transport control in heterogeneous reactions, Bircumshaw and Riddiford stated that equation 3 also applies to a rotating "paddle-type" configuration [11].

In a severe reactor accident involving melting of fuel and target elements, the primarily aluminum melt may contain uranium, lithium and fission products. These additional elements may affect the rate and nature of the steel dissolution. Mosley found that the addition of uranium tended to decrease the dissolution rates [8]. In a different analysis by Mosley and Holder, Al-Li alloy was melted in stainless steel vessels [12]. The lithium component volatilized and was deposited as a lithium oxide on the thermocouple above the melt. Leader performed a qualitative test to examine the behavior of an aluminum, uranium and lithium melt contained in a stainless steel vessel [13]. A compound containing lithium appeared to form on the top surface of the melt. Additional work is planned by Leader to further examine the roles of these three constituents in the dissolution of stainless steel at elevated temperatures.

In the proposed reactor design, inlet tubes and lateral support structures are to be fabricated using borated stainless steel. If the dissolution of the borated stainless steel elements occurred preferentially, degradation of the reactor vessel might be inhibited because of the increase of stainless steel concentration in the melt [14-15]. No literature was available on the interaction of borated stainless steel with molten aluminum.

The dissolution of stainless steel by molten aluminum is thought to be an exothermic process [16]. The energy released may play an active role in the dissolution process and should, therefore, be considered in any models examining severe reactor accident scenarios. An attempt was made to examine dissolution reactions using differential thermal analysis (DTA). However, no discernible reactions between aluminum and stainless steel were observed in this analysis.

Liquid Metal Embrittlement (LME)

Liquid metal embrittlement (LME) is a type of catastrophic failure in which an otherwise ductile metal undergoes sudden brittle fracture when coated with a thin film of a liquid metal and subsequently stressed in tension [17]. The failure occurs most often by intergranular fracture with no change in the flow behavior of the solid metal. The fracture can also occur well below the yield stress of the metal. Thin liquid metal films of a few microns or even atoms can lead to embrittlement. A number of factors appear to increase the probability of embrittlement, however, exceptions to these conditions are commonplace [18]. In general, embrittlement couples exhibit both limited mutual solubility for the solid metal and liquid metal and little tendency to form intermetallic compounds [19]. A high stress state and the presence of stress concentrators (such as pre-existing flaws) also increases the potential for embrittlement. Embrittlement by liquid metals can also be strain rate sensitive where in some instances LME is only observed at high strain rates [17]. Finally, LME is typically more prevalent at temperatures near the melting point of the liquid metal [17].

The embrittlement of austenitic stainless steels by zinc has received considerable attention from both a basic research and industrial perspective [20]. It is generally considered that molten aluminum causes corrosion of austenitic stainless steels and that the interaction will not likely cause liquid metal embrittlement [20]. The relatively high solubilities of the major stainless steel components in aluminum tends to discredit aluminum and stainless steel as a "classical" liquid metal embrittlement couple. However, because of the variability in liquid metal embrittlement occurrence and the obvious catastrophic nature of an LME failure, it was deemed important to assess the susceptibility of stainless steel to embrittlement by molten aluminum as part of this study.

A thermo-mechanical testing device is an often used instrument to assess liquid metal embrittlement susceptibility [21-22]. This apparatus was used by Savage, et al. to examine the susceptibility of the heat effected zone of type 304 stainless steel weld samples to LME by copper [22]. A marked decrease in time to failure was evident in Cu plated specimens clearly indicating the onset of embrittlement.

Assessment of the Literature

The review of the literature provided significant information regarding dissolution mechanisms and variables affecting dissolution rates. However, this data was insufficient in several key areas to accurately assess the interaction of stainless steel and molten aluminum in postulated severe reactor accident conditions. The lack of a) experimental data for dissolution of stainless steel by molten aluminum in the

temperature range of postulated severe accidents, b) dissolution data for borated stainless steels, and c) assessment of LME susceptibility of stainless steel at elevated temperatures provided the major impetus for this study.

EXPERIMENTAL PROCEDURE

Test Matrix for Dissolution Testing

A test matrix for the experimental program was developed to best examine the important variables involved in the interaction of stainless steel and molten aluminum alloys (Table I). The majority of the tests were targeted to study the interaction of type 316L stainless steel and molten 8001 aluminum alloy. Type 316L stainless steel is a readily available austenitic steel very similar in composition to the special chemistry austenitic stainless steel proposed for the heavy water NPR. Internal reactor components of concern for melting in the postulated accident scenarios are primarily composed of 8001 Al alloy with lesser amounts of uranium and lithium. Therefore, tests involving 8001 aluminum alloy were deemed to be most beneficial. Limited additional testing involving Al-U alloy was conducted to examine the effects of the uranium additions in the melt. Finally, tests involving borated stainless steel exposure to both the 8001 Al alloy and Al-U alloy provided an assessment of the effects of boron additions on dissolution.

The test matrix was divided into two sections: variable screening experiments and saturation concentration experiments. The screening experiments were designed to examine the dissolution process with varying: temperature, sample rotation (i.e. melt flow rate), stainless steel composition, and molten alloy composition. The saturation concentration experiments provided data from the extreme temperature case to calculate solute concentrations necessary for cessation of the dissolution process.

Several analytical techniques were employed to investigate the mechanisms involved in the dissolution process. These included: scanning electron microscopy (SEM) with energy dispersive spectroscopy (EDS) and x-ray diffraction (XRD).

Test Apparatus Configuration

The test apparatus used for the dissolution experiments consisted of a vertical clam-shell furnace heating an aluminum oxide crucible containing the molten aluminum alloy (Figure 1). An argon cover gas introduced above the crucible in the furnace minimized oxygen levels during the experiments. A suspended motor rotated a fixture supporting the coupon in an off-axis, circular pattern in the melt. A tantalum shaft with a tungsten

hook proved to be the best sample holder configuration (Figure 1c). During rotation tests, a digital counter was used to monitor sample rotation. The readouts on the counter included a display of the total number of revolutions and two displays of the number of revolutions/minute for alternating minute segments. The latter displays provided assurance that rotation rates were consistent for the duration of the test.

Dissolution Testing Procedure

Stainless steel immersion coupons for testing were procured from Metals Samples, Munford AL. Test coupons included Type 316L stainless steel samples (3/4" x 7/16" x 1/8") and approximately a Type 304 composition stainless steel with 1 wt % boron addition (1" x 1/2" x 1/8")*. Each coupon was individually numbered to facilitate record keeping and documentation. Certified chemical compositions were provided by the vendor for the coupons (Table II). These compositions were verified using elemental dispersive spectroscopy (EDS). Nuggets of 8001 aluminum alloy were cut from rejected outer sheaths of actual fuel elements fabricated in the 300-Area at SRS. A chemical composition record was obtained for this material and verified using EDS.

Dissolution data was obtained using a mass loss technique [23]. For static exposure tests, approximately 30 g of aluminum alloy was weighed for each series of tests involving a specific melt and placed in a 20 ml crucible. The tests involving sample rotation were performed using a 50 ml crucible containing roughly 90 g of Al alloy. Coupons were carefully weighed before exposure to the melt. The aluminum alloy was melted at approximately 800° C in the furnace under an argon cover gas to inhibit oxidation. Even though an inert atmosphere was employed, a "dross" layer formed on the molten Al surface. The melt was rapidly stirred before coupon insertion to break up this oxide layer. The temperature of the furnace was adjusted to the appropriate test temperature and allowed to stabilize. Actual test temperatures were monitored using a thermocouple following the last exposure for that series of tests. In attempt to minimize the oxide film on the stainless steel coupons and provide a uniform coupon surface finish before exposure, samples were hand-ground using 320 grit silicon carbide paper immediately prior to exposure to the melt. Typically five coupons were exposed to the same melt for each series of tests. This experimental approach provided data on dissolution rates with a "known" steel concentration in the melt. Exposure times varied depending on the test conditions and degree of attack anticipated.

* Samples used in rotation tests were cut to 1/2" lengths

Following exposure, the coupons and adhering Al alloy were weighed to account for the Al alloy removed from the melt. To remove the adhering alloy, the coupons were immersed in a 20 weight percent NaOH caustic solution. Samples were also cleaned in an HNO_3 solution to remove additional residue. In many cases, these cleaning steps were repeated to remove as much Al alloy as feasible. The samples exposed to the Al-depleted U alloy were additionally cleaned using a heated 11M HNO_3 solution to more completely remove the alloy. Coupons were then weighed to obtain final weight loss values. It was evident following the cleaning procedures that a small amount of the aluminum alloyed with the steel components and could not be completely removed from the coupons. This small additional weight is not considered significant when compared to the relative dissolved and remaining coupon weights. However, the presence of this alloyed component was a source of uncertainty in the final coupon mass measurements and made the "measured" dissolution rates less than the "actual".

Flow Visualization Experiments

The hydrodynamics of the experimental system were studied by performing flow visualization experiments. High speed video was used to ensure that laminar flow predominated in the slower speed rotation tests (10 rpm motor). The sample was rotated in water and dye was injected into the sample path. A shuttered video camera was used to acquire a progression of still pictures of the sample interaction with the dye (Figures 2a-d). The framing rate was 30 fps and the exposure time was 0.1 ms. The dye was observed to attach to the sides of the coupon at the leading edge (Figure 2b) and to detach into a single stream at the trailing edge of the coupon (Figure 2d). This behavior indicated that laminar flow conditions obtain on the wetted surfaces of the coupon and that there was virtually no vortex formation from the trailing edge of the coupon. The Reynolds number in these experiments was approximately 170 based on the streamwise dimension of the coupon [24]. The corresponding Reynolds number in the molten aluminum for the same rotational speed and coupon size was about twice this value due to the lower value of the kinematic viscosity. This Reynolds number insures that the flow characteristics for the dissolution testing were similar to those in the water flow experiments mentioned above since they are both well within the laminar flow regime [24].

The Reynolds number for tests performed in molten aluminum at 58 rpm was roughly 2000. The characteristic flow corresponding to this value is in the "transitional regime" (i.e. between laminar and turbulent flow). Flow visualization analysis of dye in water at this rotational speed showed some separation and relatively rapid diffusion of the dye indicating a transition towards turbulent flow.

Test Matrix for Liquid Metal Embrittlement (LME) Susceptibility Testing

The liquid metal embrittlement (LME) susceptibility tests were designed to qualitatively examine the interaction of molten aluminum and stainless steel in the presence of an applied stress. A number of variables, historically known to affect the probability of LME, were incorporated in the test matrix (Table III). These included: varying temperatures (concentrating near the melting point of the 8001 Al alloy), varying loads in constant load tests and varying strain rates in strain rate controlled experiments. Using these conditions, uncoated and Al coated specimens were tested using a Gleeble 1500 Thermo-mechanical Testing Device. Additionally, fractography was performed on representative samples using optical microscopy and scanning electron microscopy (SEM).

LME Testing Procedure

A procedure was developed to coat the 316L stainless steel tensile specimens with a band of 8001 aluminum alloy [25]. The technique involved dipping the samples (3/16" diameter x 4" long) in molten aluminum under optimized conditions to achieve consistent coating and wetting of the samples.

A Gleeble 1500 Thermo-mechanical Testing Device was used for the elevated temperature tensile testing. The experiments were computer controlled based on the appropriate test matrix conditions. Temperature, load and displacement data were monitored and acquired continuously throughout the tests.

RESULTS AND DISCUSSION

Dissolution Rates

The test matrix design allowed for the examination of a number of variables affecting the dissolution process. These included: temperature, flow rate, constituent solubility, molten alloy composition and stainless steel composition. The dependence of dissolution on these variables will be discussed individually in this section. In general, the data was correlated well with the varying conditions. Some variation in data from test to test was evident likely due to oxide film variations on the steel samples. This made it difficult to "fit" curves to data sets resulting in the use of scatter plots to present much of the data. Although some spurious results from test to test occurred , replicate tests showed that the experimental data generally deviated less than 20%. Additionally, some effort was made to relate the results to theoretical relationships as

described in the "Literature Survey". However, due to the status of the NPR program an elaborate theoretical assessment (i.e. similar to Dybkov [2]) was not deemed appropriate. The data does allow for such a future treatment.

Influence of Melt Temperature

Substantial increases in dissolution rates for the 316L and 304 + 1 wt % B stainless steel samples occurred with increasing melt temperatures (figure 3). The dissolution rates increased consistently (approximately an order of magnitude for each increase of 200° C) in the temperature range from 700 to 1100° C.

Although only a limited amount of varying test temperature data was available, the dissolution rates correlated relatively closely to an Arrhenius relation (equation 2). Plots of ln dissolution rate vs 1/T showed linear correlation coefficients (r^2) of 0.998, 0.992 and 0.905 for static 316L samples, static 304 + 1wt % B samples and 1 cm/s rotated 316L coupons, respectively (figure 4).

Influence of Melt Flow Rate

Increase in dissolution rates were also evident for increases in sample rotation (melt flow rate). For 900° C exposures, an approximate two fold increase in dissolution rates occurred following sample rotation at linear velocities of 1 cm/s (figure 5). An additional increase in dissolution rate of approximately 50% was observed as the rotation speed was increased from 1 to 6 cm/s. In 1100° C exposure tests, dissolution rates for samples rotated at 1 cm/s were 2 to 3 times greater than comparable static samples (figure 6). In comparing rotation tests at 1100° C, the 6 cm/s samples showed an overall slight increase in dissolution rates over the 1 cm/s samples. However, data overlap also is evident from figure 6.

Influence of Stainless Steel Concentration in Melt

The rate of dissolution generally decreased as the concentration of dissolved elements from the steel increased in the aluminum melt. However, due to the variability from test to test and since most tests were conducted well below the saturation concentrations these decreases were typically not dramatic. In 700 and 900° C exposures, only slight decreases in dissolution rates were evident with increasing steel concentration in the melt (figure 5). In the 1100° C exposures, no significant decrease in dissolution rates were observed until the steel concentration in the melt reached the solubility limit (figures 6). The changes in the dissolution rates with increasing exposure time was more evident when the data was plotted as concentration of steel in the melt vs.

cumulative exposure time (figures 7 and 8). Calculated saturation concentrations for 316L and 304 + 1 wt % B in 8001 Al alloy at 1100° C were 31 and 40 wt %, respectively. Upon sectioning of the melt containing the borated steel, an undissolved piece of steel was found partially explaining the difference in the saturation values. Further discussion of the saturation concentration results is included in the "Mechanism Analysis Section".

Influence of Depleted U in Molten Alloy

An assessment of the effect of uranium additions in the aluminum alloy was achieved by performing a series of static tests in Al - 18 wt % depleted U alloy. A consistent decrease in dissolution rates corresponded to the addition of depleted uranium in the melts (figure 9). This is consistent with the work conducted by Mosley [8]. At 1100° C an Al-U alloy containing 18 weight percent U melts as a two constituent (i.e. Al and U) system [26]. Lower dissolution rates in the Al-depleted U alloy were, thus, not surprising since the solubilities of the major constituent stainless steel elements in uranium are significantly lower than their respective solubilities in Al at 1100° C [26].

Influence of Boron Additions in Stainless Steel

As previously mentioned, a series of experiments were conducted to examine the rate of attack of aluminum on borated stainless steel. Considering the experimental error associated with the dissolution tests, no significant differences in dissolution rates were observed in comparable experiments (figures 10 and 11). The microstructural analysis revealed that the basic attack mechanisms on the two stainless steel compositions were similar. A more detailed discussion follows in the next section of this report.

Mechanism Analysis

Macroscopic Analysis

Macroscopic examination revealed some qualitative, visual information regarding the dissolution process for the various test conditions. As previously discussed, the nature and extent of attack greatly depended on exposure temperature. Generally, pitting attack was seen in the lower temperature exposures while more general corrosion was found in samples exposed at 1100° C (figure 12). The protective oxide film, which rapidly forms on austenitic stainless steels, inhibited wetting of the steel by the liquid aluminum. Attack appeared to occur locally in areas where the film was easily penetrated. Examination of short term exposure samples, however, revealed that the

attack in the 1100° C tests likely also began preferentially (figure 13). In extended exposures at high temperatures, the attack appeared "general" because of extensive growth of the initial pits. In extreme cases this led to nearly complete or total consumption of the test specimens (figure 13).

In this study, attempts were made to minimize the protective oxide film on the steel, however, significant variability in attack on the coupons was still observed. It is anticipated that oxide films will be present on both the aluminum and stainless steel during reactor operation. In fact, previous SRS reactor experience showed that an adherent hydrated aluminum oxide film or turbidity deposits on stainless steel components during reactor operation in addition to the chromium oxide film. Therefore, in general, wetting of the steel by the aluminum will be inhibited leading to relatively slow dissolution. However, if the severe accident scenario involves any process which may disrupt the oxide films on the steel it is difficult to ensure that dissolution will not occur rapidly in localized vessel locations. In this event, additional study may be necessary to assess the likelihood of oxide film removal and subsequent breaching of the reactor vessel. Furthermore, the variability from test to test (mainly due to the oxide film variations) causes some doubt into the accuracy of the dissolution rate values. It may therefore be beneficial to perform some limited additional experiments using environmentally controlled test apparatus. The scope of these experiments could be limited to specified "worst-case" severe accident conditions and scaled appropriately.

The effect of increased stainless steel concentration in molten aluminum over time was evident by examining a series of coupons exposed to the same melt (figure 14). Significant variation from test to test was evident, however, following the fifth exposure little or no attack occurred indicating the saturation concentration was likely reached. The increase in dissolution rate with an increase in flow rate was also visually evident when examining coupons exposed to the various flow conditions (figure 15).

Microstructural and Mechanism Analysis - 700 and 900° C Exposures

Metallographic sections of samples exposed to the various melt conditions provided more detailed information regarding the effects of temperature and oxide films on the steel on dissolution. Figures 16 and 17 show the surfaces of static samples exposed to 8001 Al melts at 700 and 900° C, respectively. The SEM afforded the depth of field necessary to see the pitting prevalent in the 700° C exposures (figure 16). Although a more general attack was typical in the samples exposed at 900° C (figure 17), regions where the oxide film inhibited wetting were evident. The formation of intermetallic

compounds at the interface was also more pronounced in the samples immersed in the 900° C melts.

In an effort to gain insight into the mechanisms involved in the dissolution process, SEM at increased magnification, elemental mapping and semi-quantitative analysis were performed on the melt/sample interface regions of a 316L sample exposed to 8001 Al alloy at 900° C. A two phase interface region formed during the interaction (figure 18). The elemental maps clearly showed the formation of an Al-Fe rich intermetallic phase extending in a "finger-like" fashion into the molten aluminum (figure 19). Between the steel and this region, a thin (~ 1 um) interfacial layer was evident which was again Al and Fe rich but also contained significantly more chromium than the "finger-like" phase. It is hypothesized that the "finger-like" layer forms rapidly after steel exposure to Al and limits the diffusion of Cr into the aluminum. This is supported by the relative depletion of Cr in the "finger-like" (Al-Fe rich) phase. The nickel appeared relatively homogeneously dispersed throughout the interfacial layers including the "finger-like" layer and does not appear to actively form nickel-rich intermetallic compounds. A "tube shaped", chromium rich intermetallic phase protruded from the extremities of the "finger-like" layer into the melt.

It is speculated that the dissolution process may occur by an alternating 2 part process involving migration of iron and chromium. In this process, the "finger-like" (Al-Fe rich) phases grow to a critical size and break-off into the melt. During the growth period of the Al-Fe rich "fingers", the formation of Al-Cr intermetallic phases is inhibited. However, when the Al-Fe rich phases are mechanically separated from the interface the chromium is "free" to migrate and form intermetallic compounds. It is thought that the unique "tube-shaped" intermetallic phases either formed immediately after separation of the "finger-like" phases and moved away from the interface with subsequent growth of new "fingers" or formed heterogeneously on the Al-Fe rich "fingers" upon cooling of chromium-rich melt regions.

Efforts were made to identify these intermetallic phases by performing x-ray diffraction (XRD) on solid samples and crushed powder from saturated melts. The results of the XRD analysis, however, was inconclusive. Stoichiometries of the phases present could be based on Al_2Fe, Al_3Fe and deviations to the latter structure such as $Al_{13}Fe_4$ and $Al_{76.8}Fe_{24}$. It is very difficult to draw definitive conclusions for a few reasons. Overlap of the major peaks occur in the characteristic patterns of these phases and shift of the peaks is likely due to the substitution of Cr and Ni for iron in the structures. Similar difficulties in phase identification were encountered by Dybkov [2]. In this work, XRD and electron microprobe were performed on a carefully prepared sample of the two interface layers (i.e. similar to the interfacial layers in the 900° C

exposures). The layer closest to the aluminum was said to be based on the $AlFe_3$ intermetallic and the compact layer closest to the steel based on the Al_2Fe_5 phase. Since alloying with Cr and Ni was obvious these compounds were written as $Al(Fe,Cr,Ni)_3$ and $Al_2(Fe,Cr, Ni)_5$.

Similar elemental maps on borated steel samples exposed to 8001 Al provided insight into the behavior of the boron constituent during the dissolution process. In the borated steel, the boron combines with Cr to form insoluble chromium-boride precipitates. During the dissolution process, the chromium-boride precipitates remain insoluble and pass as solids into the melt (figure 20). The Al-Fe rich "finger-like" layer was relatively depleted of the borides and Al-Cr-B rich compounds appeared to form heterogeneously on the Al-Fe rich phases. Many chromium-rich compounds of the approximate size of the chromium borides were also observed in the melt. It was not possible to discern whether these were unreacted chromium boride compounds or also Al-Cr-B intermetallic phases. The borated steel structural components, in addition to providing an operational function, are also designed to prevent recriticality in the reactor in certain accident scenarios. Therefore, the fact that the boron remains in the melt during the dissolution process is very important from a safety standpoint.

Microstructural and Mechanism Analysis - 1100° C

Analysis of samples exposed to melts at 1100° C, indicated that a dual-diffusion mechanism prevailed. In this case, diffusion of constituent steel atoms into the aluminum and diffusion of Al into the steel appeared to occur simultaneously. Figure 21 shows the interface region of a 316L sample exposed to 8001 Al for 1 minute at 1100° C. In this very short-term exposure, a dual-phased interface was "frozen" as it progressed across the stainless steel coupon. The two interfacial layers were of approximately the same size. Elemental maps of the interface region showed that the layer which formed on the aluminum-rich side (left side) was rich in Fe and Ni and comparatively depleted in Cr (figure 22). The interface layer contacting the base metal (right side) showed only the presence of the primary stainless steel elements. However, it is possible that some Al was present in this layer. The aluminum may not have been observable by EDS because of the large absorption of characteristic Al x-rays by the stainless steel. The map of elemental chromium shows that Cr rich intermetallic phases also formed heterogeneously on the Al-Fe rich layer. Nickel appeared relatively well dispersed throughout the interface region. A complex array of intermetallic phases in an aluminum matrix resulted in the region behind this interface and in samples completely consumed by the aluminum (figures 23 and 24). Elemental analysis on these specimens showed that the composition of the "tube-shaped" phases

and "plate-like" (finger-like) phases had compositions similar to the intermetallic phases observed in samples exposed at 900° C. This dual-diffusion process was likely responsible for the rapid attack of the steel in the 1100° C exposures.

Analysis of Melt Regions

Elemental maps and semi-quantitative analysis of sectioned 8001 Al melts following coupon exposure substantiated many of these conclusions and provided additional information regarding the dissolution process. Analysis of areas near the top of the melt and bottom of the melt showed that elements from the steel (existing in the form of intermetallic compounds) were relatively homogeneously dispersed throughout the melts (figures 25-27). Elemental mapping and semi-quantitative analysis was performed on a saturated 8001 aluminum melt used in 1100° C exposure tests (figures 26 and 27). The maps showed that an Al-Fe rich intermetallic phase (similar in composition to the "finger-like" phase) and an Al-Cr rich "tubed-shaped" phase formed in the melt. Semi-quantitative analysis results showed that the relative elemental compositions near the top and bottom of the melt were virtually identical (Table IV). It is important to note that the concentrations of Ni and Cr in the melt are well below their respective solubilities of 30 wt % and 42 wt % in molten aluminum at 1100° C [25]. Furthermore, when the relative compositions of only the steel elements in the melt are normalized the concentrations are nearly equivalent to the composition of the stainless steel. This indicates that the dissolution process is non-selective on a macro-scale with regard to major stainless steel elements at 1100° C. This finding is consistent with the observation of Dybkov at lower melt temperatures [2].

Melt Viscosity Changes

Another important visual observation during the tests involved the apparent change in melt viscosity with an increase in concentration of stainless steel in the melt. At the culmination of the 1100° C tests (involving saturated melts), the viscosity of the melt had increased dramatically. Dybkov made reference to data compiled by Vol on the viscosity changes in molten aluminum with increasing iron concentration [2]. An increase in dynamic viscosity of 10% was observed with each additional weight percent of Fe introduced into the melt. Assuming that Cr and Ni additions have similar effects on viscosity, the saturated melts containing roughly 30 wt % stainless steel experienced a potential increase of 300% in dynamic melt viscosity. The kinematic viscosity would also increase but to a lesser extent since an increase in melt density would also occur. This increase in viscosity with concentration will significantly affect any modeling of flow behavior in reactor accident scenarios.

"Dross" Formation on Melt Surface

The character of the melt also changed with prolonged exposure to the atmosphere. Even though efforts were made to minimize oxygen concentration using a cover gas, a "dross" (aluminum oxide) layer readily formed on the melt surface. The amount of "dross" consistently increased with increasing temperature, exposure time and agitation of the melt (figure 28). In a severe accident the "dross" layer would likely insulate the melt and inhibit heat loss by convection. The effect that this would have on heat removal in the NPR reactor design in a severe accident may warrant additional study.

Liquid Metal Embrittlement (LME) Susceptibility

The susceptibility of stainless steel to embrittlement by molten aluminum was evaluated using a series of tests with varying temperatures, loads and strain rates. These variables provided a broad survey of conditions known to effect the susceptibility of metals to LME. No evidence of stainless steel embrittlement by molten aluminum was seen from these tests.

A series of constant load, stress-rupture tests were conducted at 650, 675, 700, 750 and 1100° C. These tests were concentrated around the melting temperature of the aluminum (~660° C) since LME susceptibility increases near the melting point of the embrittling metal. Generally, a decrease in time to failure was seen in coated samples as compared to uncoated specimens tested under comparable conditions (Table V). Dissolution of the test samples by the molten aluminum, either during the coating process or testing at temperature, likely caused this decrease in the time to failure because of a decreased effective cross-sectional area. Visual inspection of the test samples indicated a ductile (cup and cone) fracture mode predominated with no evidence of brittle fracture. SEM of Al coated and uncoated fracture specimens indicated some dissolution likely occurred in the coated specimens (figures 29 and 30).

The load was increased by 50% from the constant load tests to examine if an increase in stress level affected the susceptibility to embrittlement. With the increase in load, the times to failure (on the order of seconds) were similar for coated and uncoated specimens. This supports the hypothesis that dissolution caused the decrease in time to failure in the lower load stress-rupture tests since in the higher load tests there was not sufficient time for dissolution to occur. Additionally, similar to the previous tests, embrittlement of the steel by the 8001 Al was not evident as ductile fracture dominated.

At high strain rates the likelihood of LME in solid-liquid metal couples typically increases. This phenomenon was evaluated in the Al-stainless steel system in tests conducted at constant displacement rates of 1×10^{-3} in/s and 1 in/s. In these tests, both

coated and uncoated samples failed in essentially the same amount of time and ductile fracture predominated in all tests. The measured loads, however, were consistently lower for the coated specimens. In the slow displacement rate test 1×10^{-3} in/s conducted at 700° C, this difference in load was approximately 30 kg (figure 31). Assuming the samples failed at the same stress levels, a rough calculation shows that this corresponds to a decrease in sample radius of 0.005 cm. According to the dissolution rate data, this decrease in radius is about what would be expected from dissolution following sample coating at 900° C and tensile testing at 700° C.

Finally, stress-rupture tests were performed on notched specimens to ensure that fracture originated at the surface of the specimens. In these tests, no correlations regarding time to failure were achievable, likely due to variations in the cross-sectional areas of the notched samples after machining. Analysis of the fracture surfaces showed no indication that embrittlement occurred. The fracture surfaces appeared essentially identical to the unnotched samples.

CONCLUSIONS

A test program was completed to characterize the dissolution of stainless steel by molten aluminum and aluminum alloys. The following conclusions are drawn from this study:

1) Oxide films on stainless steel and aluminum inhibited dissolution and caused variability in dissolution rates and nature of attack.

2) Dissolution rates increased significantly with increasing temperatures and with melt flow rates.

3) Dissolution mechanisms and rates were generally similar for type 316L and 304 + 1 wt % B stainless steels. In borated steels, borides pass into the melt and remain insoluble.

4) Dissolution was non-selective on a macro-scale with regard to stainless steel constituent elements.

5) Uranium additions in the molten alloy decreased the steel dissolution rates.

6) Al-Fe (rich) intermetallic phases appeared to form rapidly at steel/melt interface. This interfacial layer inhibited diffusion of chromium and nickel into melt.

7) Visual observation revealed a significant increase in melt viscosity with increasing stainless steel concentration in the Al melt.

8) No convincing evidence for LME of stainless steel by molten aluminum was observed.

ACKNOWLEDGEMENTS

The technical and administrative support of D. T. Rankin was instrumental over the duration of this effort. The technical assistance of M. J. Pechersky, S. L. West and A. B. Barnes was also greatly appreciated. Dr. Pechersky assisted in the flow visualization tests and provided expertise in the analysis of the flow behavior in the experiments. Dr. West was instrumental in the definition, performance and interpretation of the liquid metal embrittlement susceptibility tests. Mr. Barnes assisted in the definition of the LME tests and developed a consistent method for coating tensile specimens with aluminum alloy. Additionally, the efforts of J. R. Durden, M. E. Summer and A. R. Jurgensen were instrumental in the materials characterization aspects of this study. J. W. Kronberg designed and fabricated the rotation counter. Finally the assistance of R. S. Garritano, F. A. Cheek, A. B. Antoniccllli and A. S. Holston in performing various aspects of the experimental work was also greatly appreciated.

REFERENCES

1. "Detailed Technical Plan for the Severe Accidents and Transient Fuel/Target Performance Task (WBS 1.9.3) - Revision 3 Preliminary Draft", NPRW-SA91-4, p II-129, August 30, 1991.

2. V. I. Dybkov, "Interaction of 18Cr-10Ni Stainless Steel with Liquid Aluminum", **Journal of Materials Science**, Vol. 25, p 3615, 1990.

3. T. N. Nazarchuk, G. T. Kabannik and V. I. Dybkov, "Kinetics of Solution of 12Kh18N10T Steel in Molten Aluminum", **Soviet Materials Science**, Vol. 21, p 413, 1985.

4. J. D. Webb and S. L. Pohlman, "Reliability and Durability Study of a Thermal Receiver Utilizing ASI Type 316 Stainless Steel in Contact with Molten Aluminum", Solar Energy Research Institute, SERI/TP-641-653, March 1980.

5. M. Niinomi, Y Ueda and M. Sano, "Dissolution of Ferrous Alloys in Molten Aluminum", **Transactions of the Japan Institute of Metals**, Vol. 23, p 780, 1982.

6. V. N. Yeremenko, Ya. V. Natanzon and V. I. Dybkov, "Interaction of the Refractory Metals with Liquid Aluminum", **Journal of Less Common Metals**, Vol. 50, p 29, 1976.

7. V. N. Yeremenko, Ya. V. Natanzon, V. I. Dybkov, "The Effect of Dissolution on the Growth of the Fe_2Al_5 Interlayer in the Solid Iron-Liquid Aluminum System", **Journal of Materials Science**, Vol. 16, p 1748, 1981.

8. W. C. Mosley, Jr., Unpublished Work, 1991.

9. P. F. Tortorelli, "Fundamentals of High-Temperature Corrosion in Liquid Metals", **Metals Handbook, 9th Edition, Volume 13: Corrosion**, ASM International, Materials Park, OH, p 56, 1987.

10. J. C. Marra, "Degradation of 316L Stainless Steel by Molten Aluminum", to be published in **Microstructural Science, Vol. 19**, 1992.

11. L. L. Bircumshaw and A. C. Riddiford, "Transport Control in Heterogeneous Reactions", **Quarterly Reviews, London: The Chemical Society**, Vol VI, p 157, 1952.

12. J. S. Holder, "Li-Al Vaporization & Deuteration Experiment (U)", Westinghouse Savannah River Co., SRT-HTS-92-0089, July 8, 1992.

13. D. R. Leader, Unpublished Work, 1992.

14. Discussions at First Severe Accident Technical Information Exchange Meeting, New York, October 16, 1991.

15. D. H. Cho memorandum to K. D. Bergeron, "Masses of Borated Inlet Tubes and Lateral Support Structure ("Black Forest") in Lower Plenum", Argonne National Laboratory, Argonne IL, October 25, 1991.

16. D. A. Powers memorandum to K. D. Bergeron, "Heat of Solution of Fe in Al", Sandia National Laboratories, Albuquerque, NM, November 1992.

17. M. H. Kamdar, "Liquid Metal Embrittlement", **Metals Handbook, 9th Edition, Volume 13: Corrosion**, ASM International, Materials Park, OH, p 171, 1987.

18. W. Rostoker, J. M. McCaughey and H. Markus, **Embrittlement by Liquid Metals**, Reinhold Publishing Corporations, New York, p 15, 1960.

19. A. R. C. Westwood and R. M. Latanision, "Absorption-Induced Embrittlement by Liquid Metals", **Corrosion by Liquid Metals**, Edited by J. E. Draley and J. R. Weeks, Plenum Press, New York, p 405, 1970.

20. C. P. Dillon, "Liquid Metal Cracking of Stainless Steels in Chemical Plants", **Materials Selection and Design**, p 54, November 1990.

21. M. H. Kamdar, "Liquid Metal Embrittlement", **Metals Handbook, 9th Edition, Volume 11: Failure Analysis and Prevention**, ASM International, Materials Park, OH, p 233, 1987.

22. W. F. Savage, E. F. Nippes and M. C. Mushala, "Liquid-Metal Embrittlement of the Heat-Affected Zone by Copper Contamination", **Welding Research Supplement**, p 237-s, August 1978.

23. J. C. Marra, "Dissolution Testing of Stainless Steel in Molten Aluminum", Westinghouse Savannah River Co., TP-92-018 Rev. 1, August 21, 1992.

24. H. Schlichting, **Boundary Layer Theory**, McGraw Hill Book Company, Inc., New York, p 17, 1951.

25. A. B. Barnes, "Liquid Metal Embrittlement (LME) Susceptibility of Stainless Steel by Molten Aluminum - Test Development (U), Westinghouse Savannah River Co., SRT-MTS-92-4035, August 6, 1992.

26. T. B. Massalski, Editor-In-Chief, **Binary Alloy Phase Diagrams, Second Edition**, Volume 1, ASM International, Materials Park, OH, p 138, 1990.

TABLE I

TEST MATRIX FOR DISSOLUTION TESTING

8001 Al Alloy

Stainless Steel Type	Temp. (°C)	Rotation	Exposures with Melt	Replicate
316L	700	Static	5	no
316L	900	Static	5	yes
316L	1100	Static	10*	yes
316L	700	1 cm/s	5	no
316L	900	1 cm/s	5	yes
316L	900	6 cm/s	5	no
316L	1100	1 cm/s	7	yes
316L	1100	6 cm/s	6	no
304 + 1 wt % B	700	Static	5	no
304 + 1 wt % B	900	Static	5	no
304 + 1 wt % B	1100	Static	5*	no
304 + 1 wt % B	900	1 cm/s	5	no
304 + 1 wt % B	1100	1 cm/s	5	no

Al-18 wt % Depleted U Alloy

Stainless Steel Type	Temp. (C)	Rotation	Exposures with Melt	Replicate
316L	900	Static	5	no
316L	1100	Static	5	no
304 + 1 wt % B	1100	Static	5	no

* These tests provided saturation concentration data at 1100° C

TABLE II

CHEMICAL COMPOSITIONS OF STAINLESS STEEL COUPONS

	Weight Percent of Element	
Chemical Element	316L Stainless Steel	304L + 1% B Stainless Steel
Aluminum	-	-
Boron	-	1.02
Carbon	0.025	0.050
Chromium	16.88	18.44
Cobalt	0.18	0.059
Copper	0.11	-
Iron	Balance	Balance
Manganese	1.70	1.66
Molybdenum	2.20	0.072
Nickel	10.98	13.48
Nitrogen	0.017	-
Phosphorus	0.044	0.020
Sulfur	0.029	0.009
Silicon	0.42	0.54

TABLE III

TEST MATRIX FOR TENSILE TESTS TO DETERMINE LIQUID METAL EMBRITTLEMENT SUSCEPTIBILITY*

Temperature (C)	Load (kg)	Strain rate (ips)
650	562	-
675	515	-
700	425	-
750	380	-
1100	60	-
650	843	-
675	773	-
700	638	-
750	570	-
1100	90	-
650	-	.001
675	-	.001
700	-	.001
750	-	.001
1100	-	.001
650	-	1
675	-	1
700	-	1
750	-	1
1100	-	1

* All tests conducted on uncoated samples and samples coated with 8001 Al alloy.

TABLE IV

SEMI-QUANTITATIVE ELEMENTAL
ANALYSIS RESULTS OF MELT
SATURATED BY 316L STAINLESS STEEL

Region Near Top of Melt

Element	Concentration	Normalized Steel Concentration	Steel Specification Concentration*
Aluminum	66.40 wt %	-	-
Iron	22.66 wt %	67.42 wt %	67.26 wt %
Chromium	5.93 wt %	17.64 wt %	16.88 wt %
Nickel	5.02 wt %	14.93 wt %	10.98 wt %

Region Near Bottom of Melt

Element	Concentration	Normalized Steel Concentration	Steel Specification Concentration*
Aluminum	67.13 wt %	-	-
Iron	23.01 wt %	70.00 wt %	67.26 wt %
Chromium	5.61 wt %	17.06 wt %	16.88 wt %
Nickel	4.25 wt %	12.93 wt %	10.98 wt %

* Vendor specification data (see Table II)

TABLE V

TIME TO FAILURE FOR CONSTANT LOAD
STRESS-RUPTURE SPECIMENS

Temperature (° C)	Force (kg)	Time to Failure (min)	Sample Type
650	562	52	uncoated
650	562	45	uncoated
650	562	45	uncoated
650	562	22	coated
650	562	26	coated
675	515	33	uncoated
675	515	19	uncoated
675	515	5	coated
675	515	5	coated
700	425	25	uncoated
700	425	5	coated
750	380	20	uncoated
750	380	5	coated
1100	70	5	uncoated
1100	70	2	coated
1100	60	21	uncoated
1100	60	13	uncoated
1100	60	12	uncoated
1100	60	13	coated
1100	60	8	coated
1100	60	4	coated

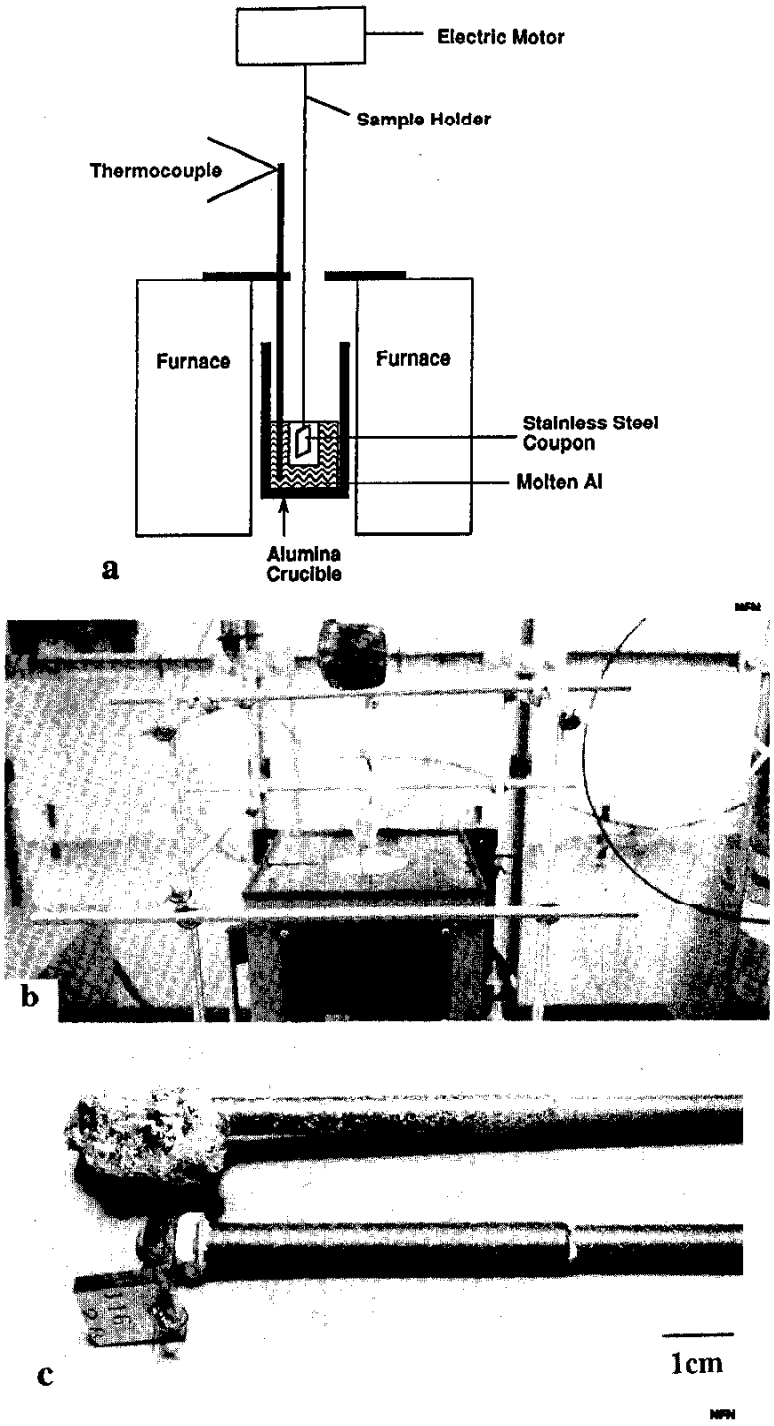

Figure 1. Equipment configuration and apparatus for dissolution testing.

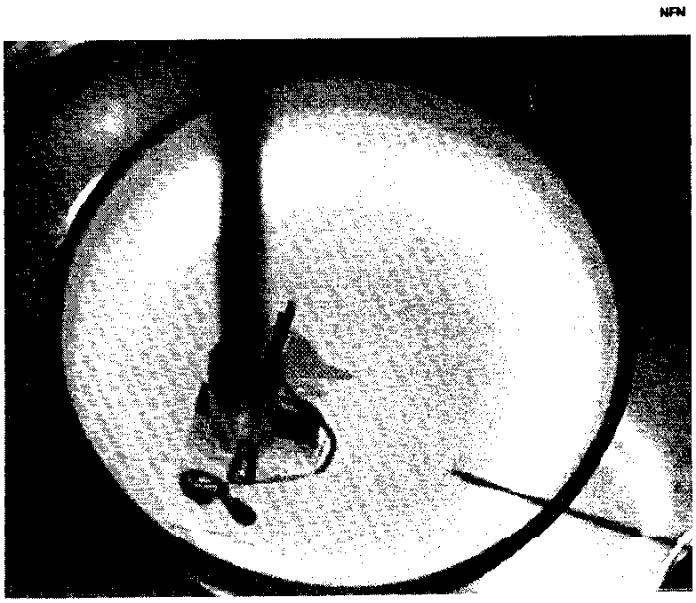

Figure 2a. Flow visualization experiment where leading edge of coupon met dye stream.

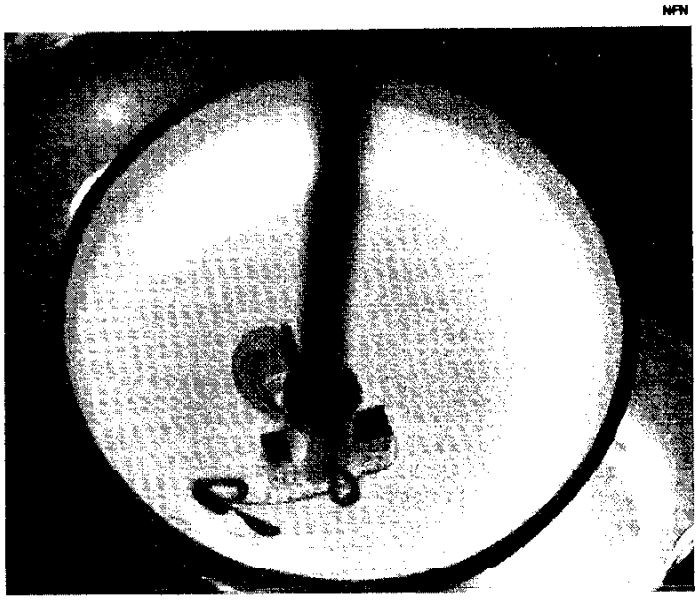

Figure 2b. Continuation of flow visualization where dye attached to sides of coupon.

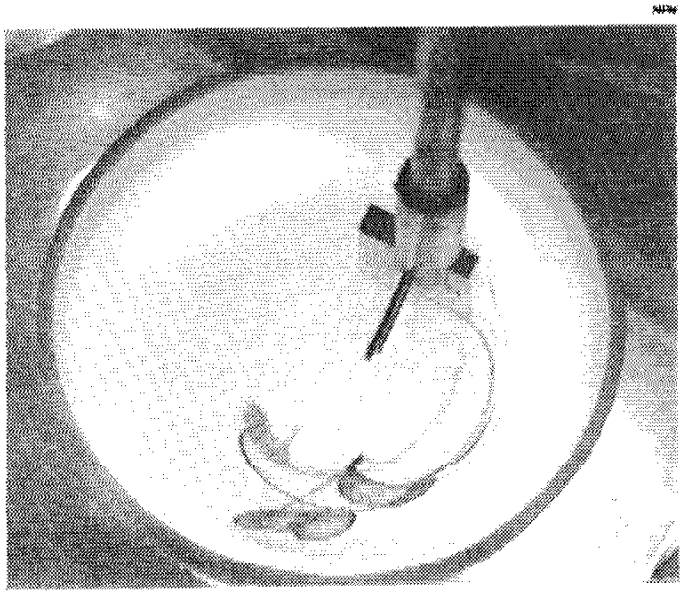

Figure 2c. Continuation of flow visualization experiment. Dye remained attached to coupon sides and converged at trailing edge.

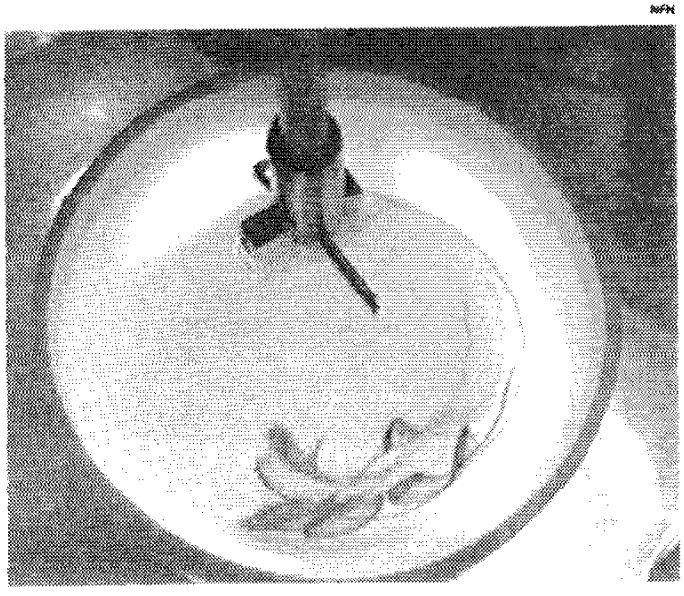

Figure 2d. Culmination of flow visualization experiment. Dye detached at trailing edge into a single stream with essentially no vortex formation.

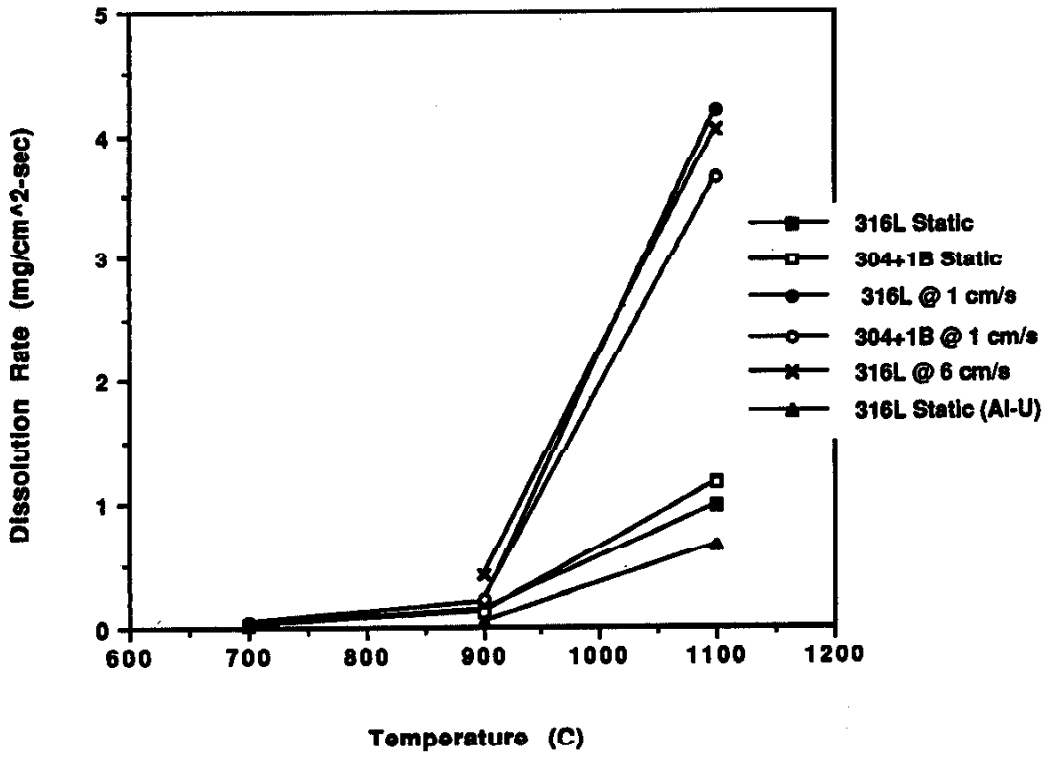

Figure 3. Maximum dissolution rate vs. exposure temperature for samples tested under the various experimental conditions. Data points are connected to facilitate comparison of data sets.

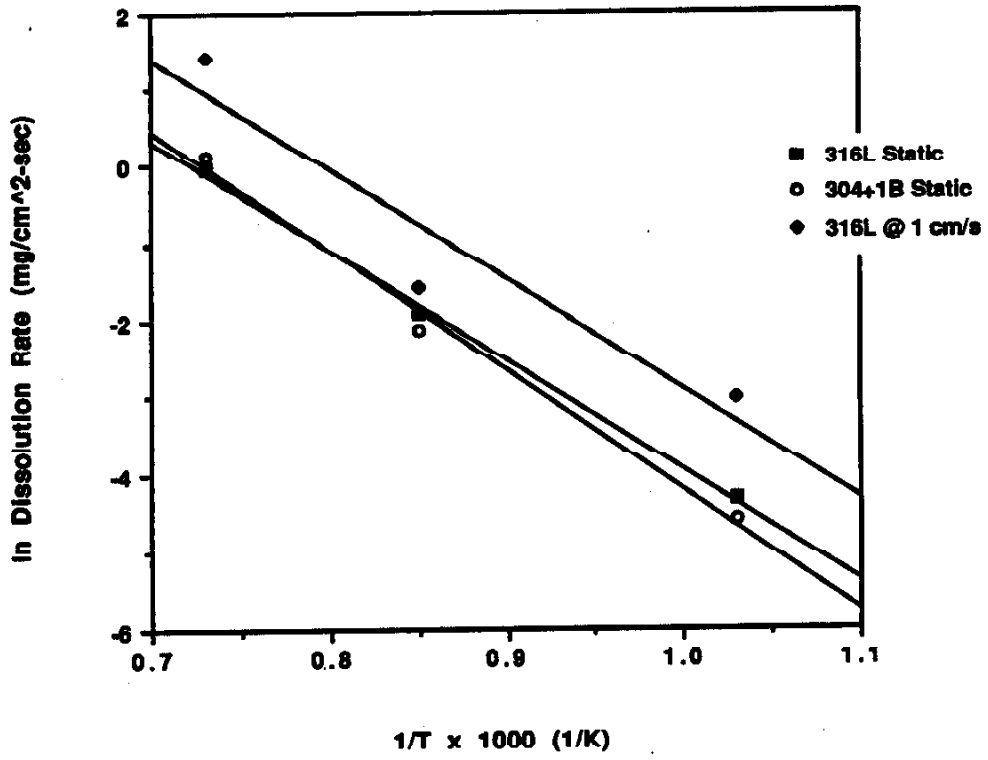

Figure 4. Relation of ln dissolution rate and 1/T showing Arrhenius type behavior exhibited by the dissolution of stainless steel by molten aluminum.

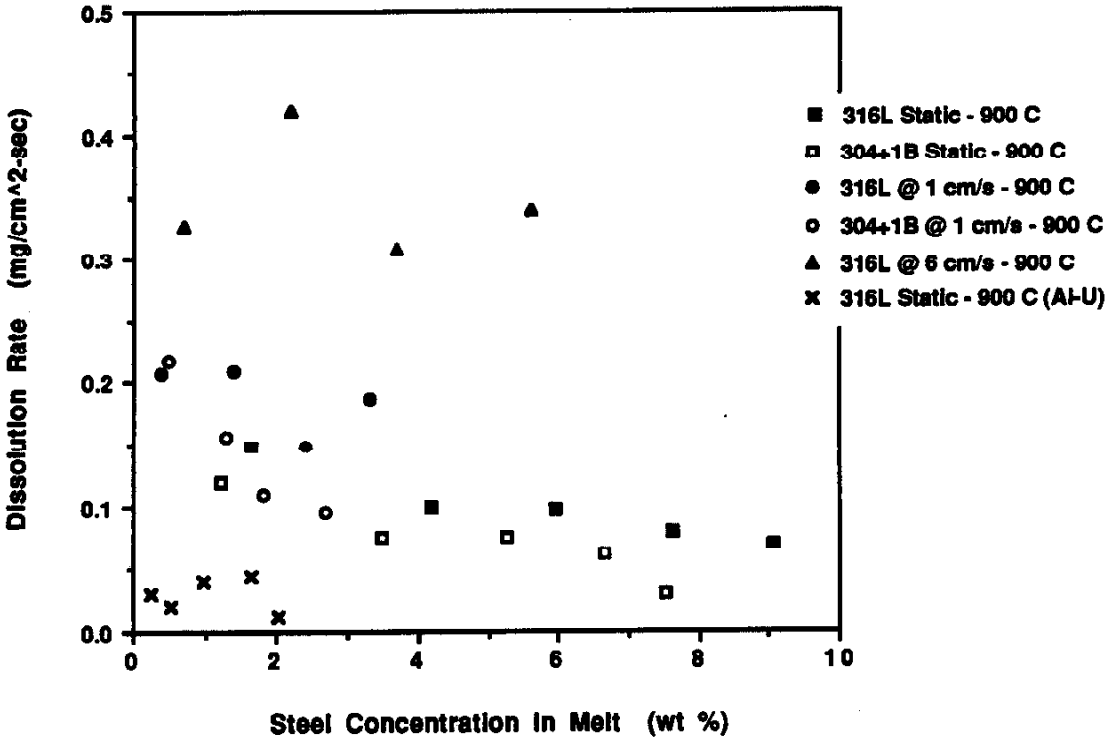

Figure 5. Dissolution rate vs. average concentration of steel in the melt for samples exposed at 900° C.

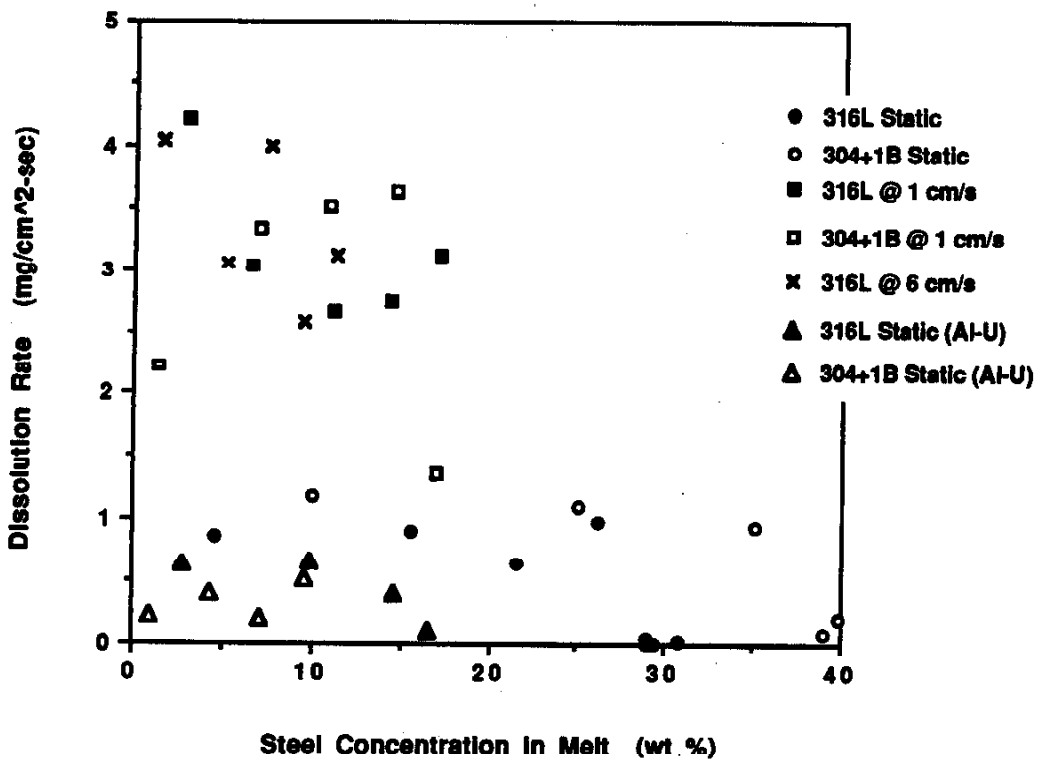

Figure 6. Dissolution rate vs. average concentration of steel in the melt for samples exposed at 1100° C.

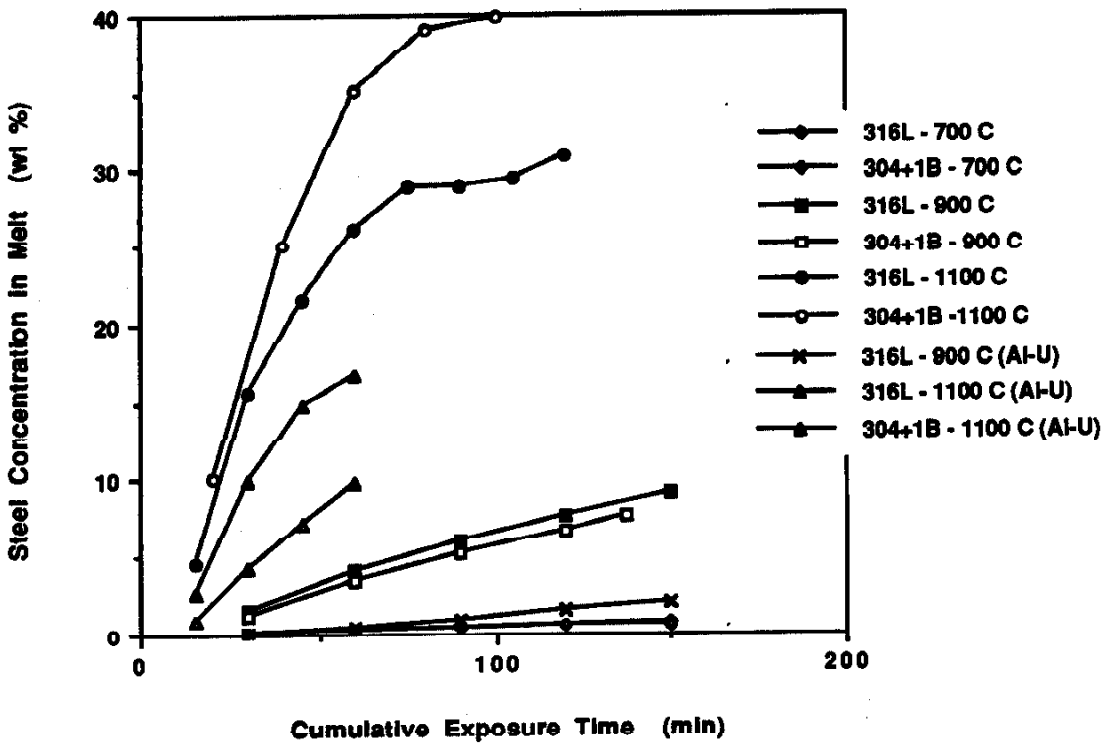

Figure 7. Relation of average steel concentration in the aluminum melt and cumulative exposure time for static exposed samples. Data points are connected to facilitate comparison of data sets.

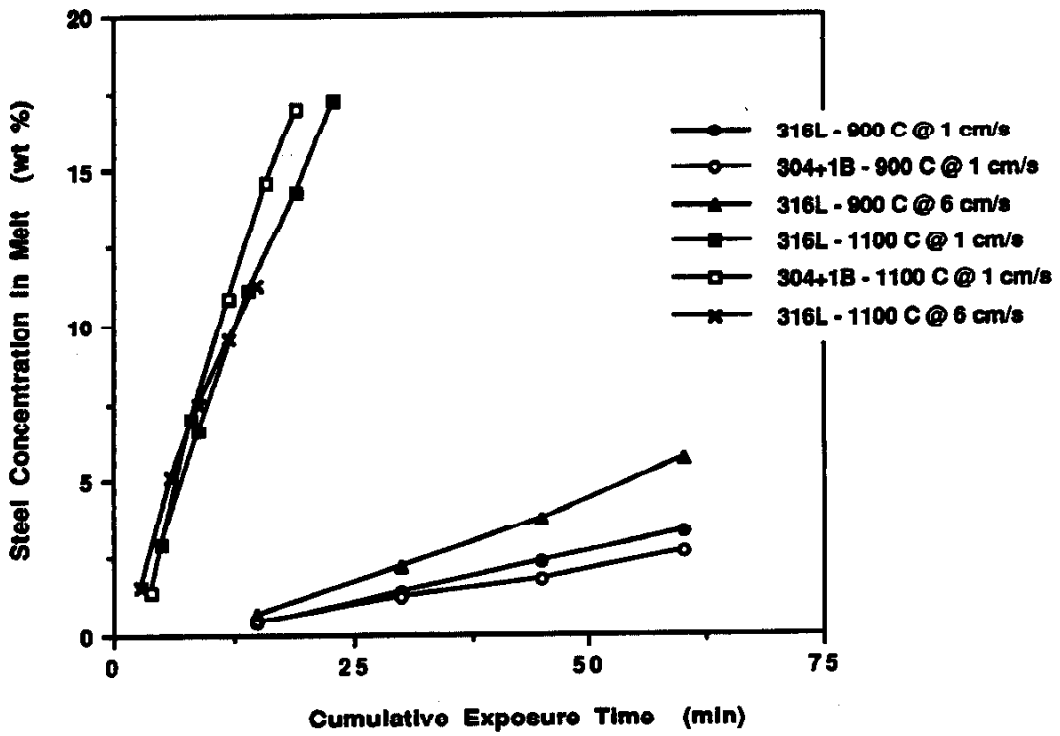

Figure 8. Relation of average steel concentration in the melt and cumulative exposure time for samples rotated in 8001 Al alloy. Data points are connected to facilitate comparison of data sets.

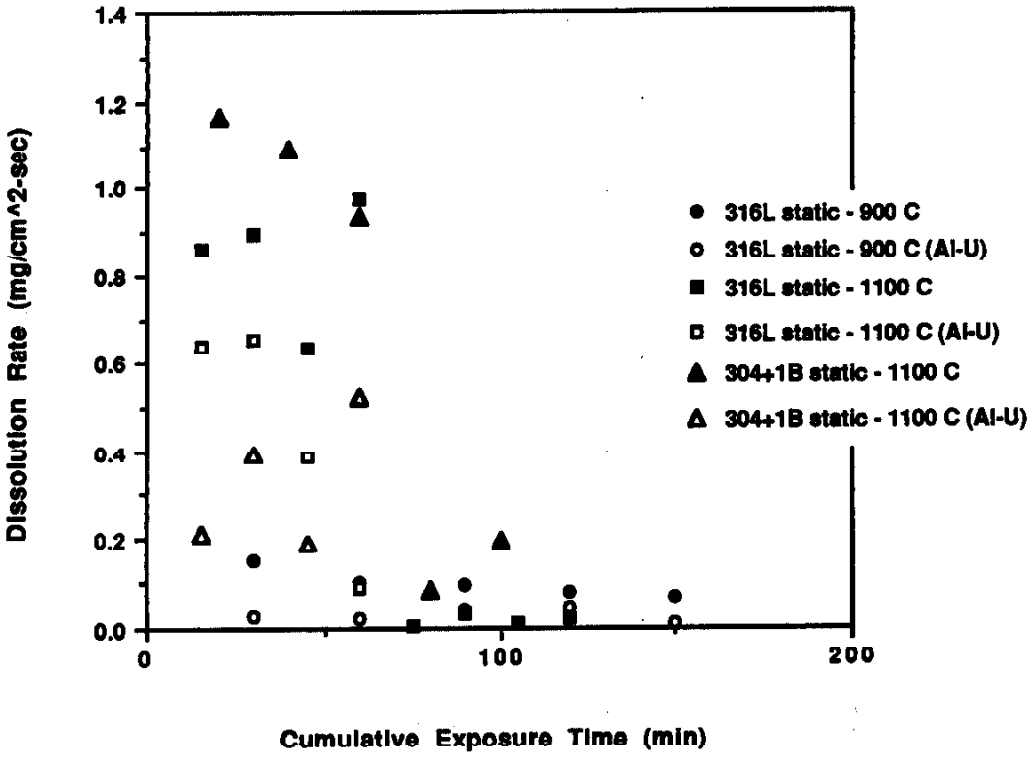

Figure 9. Relation of dissolution rates and cumulative exposure times for stainless steel samples exposed to 8001 Al alloy and Al-18 wt% depleted U alloy under comparable experimental conditions.

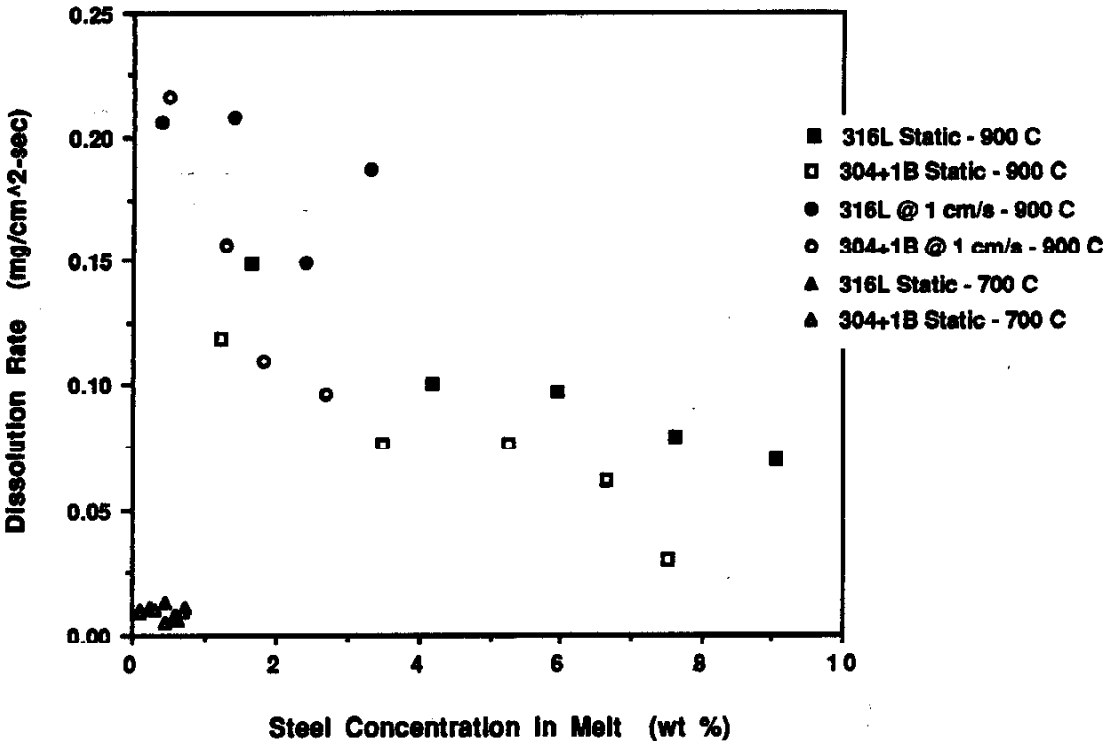

Figure 10. Dissolution rate vs. average steel concentration in the melt for 316L and 304 + 1 wt % B stainless steel samples exposed under comparable conditions at 700 and 900° C.

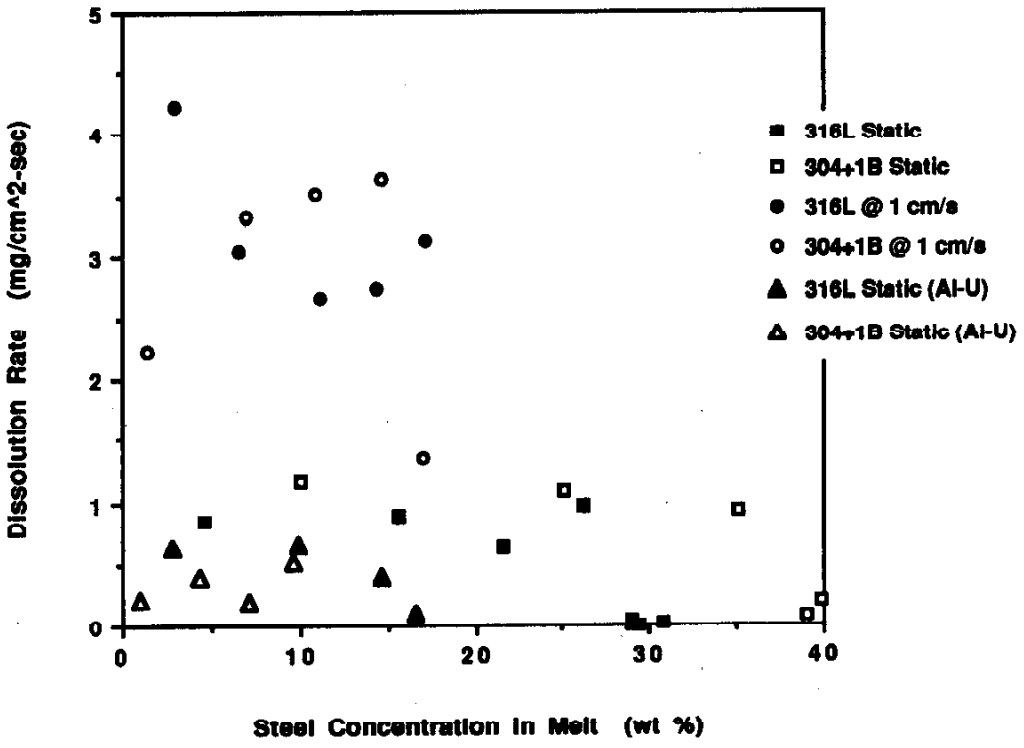

Figure 11. Dissolution rate vs. average steel concentration in the melt for 316L and 304 + 1 wt % B stainless steel samples exposed under comparable conditions at 1100° C.

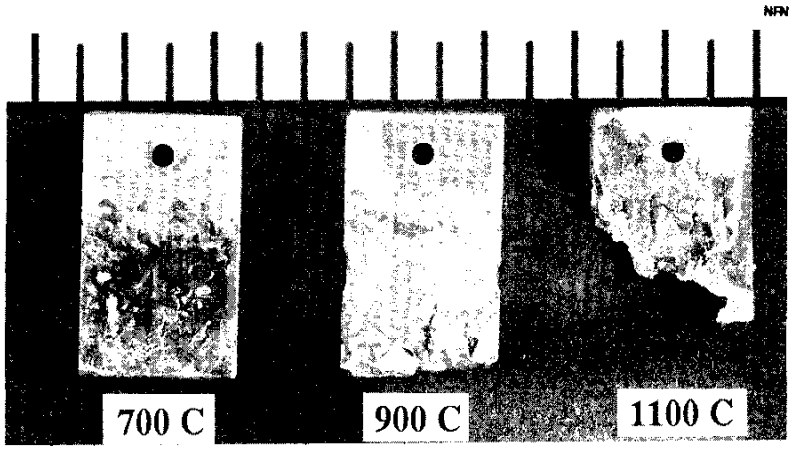

Figure 12. Typical 316L samples following static exposures at 700, 900 and 1100° C.

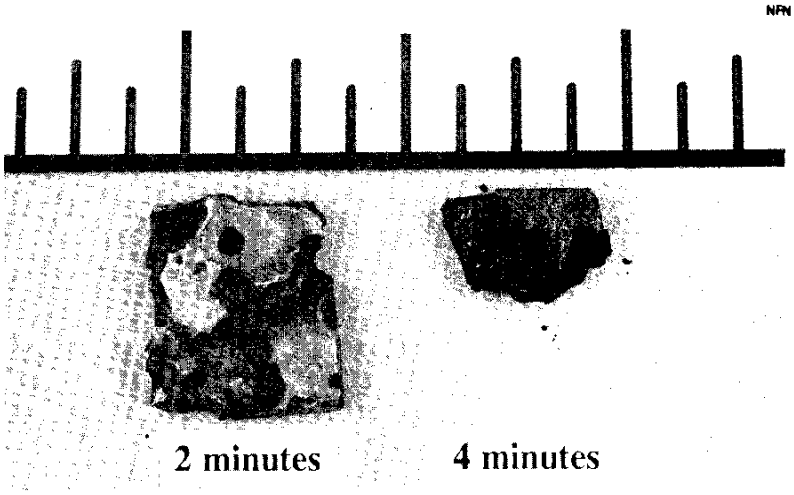

Figure 13. Type 316L stainless steel samples following rotation at 1 cm/s in an 1100° C melt for 2 minutes and 4 minutes. Note preferential attack in sample exposed for 2 minutes.

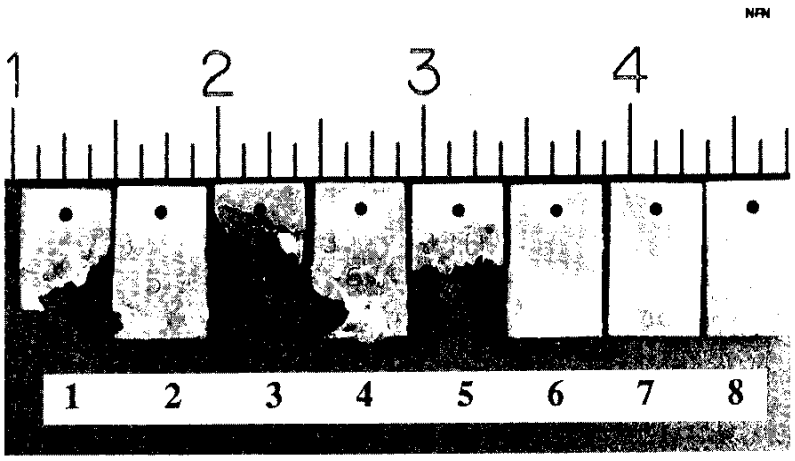

Figure 14. Series of 316L samples following static exposure at 1100° C. Note cessation of dissolution in 6, 7 and 8 coupons.

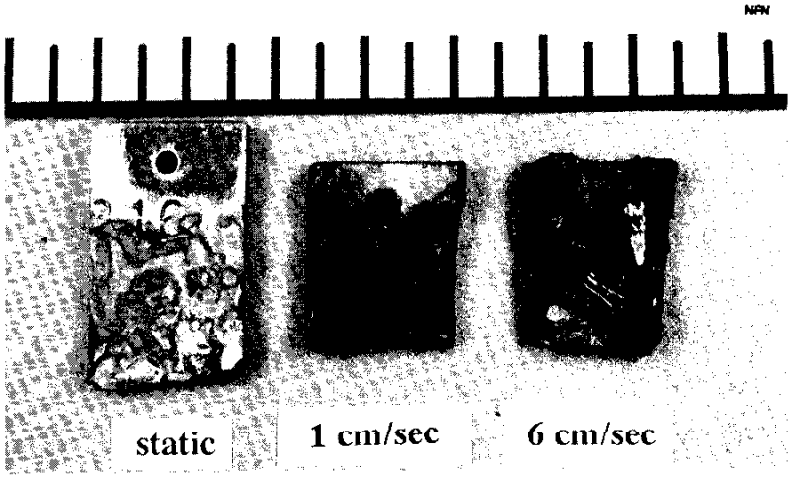

Figure 15. Type 316L coupons following exposure at 900° C under various melt flow conditions.

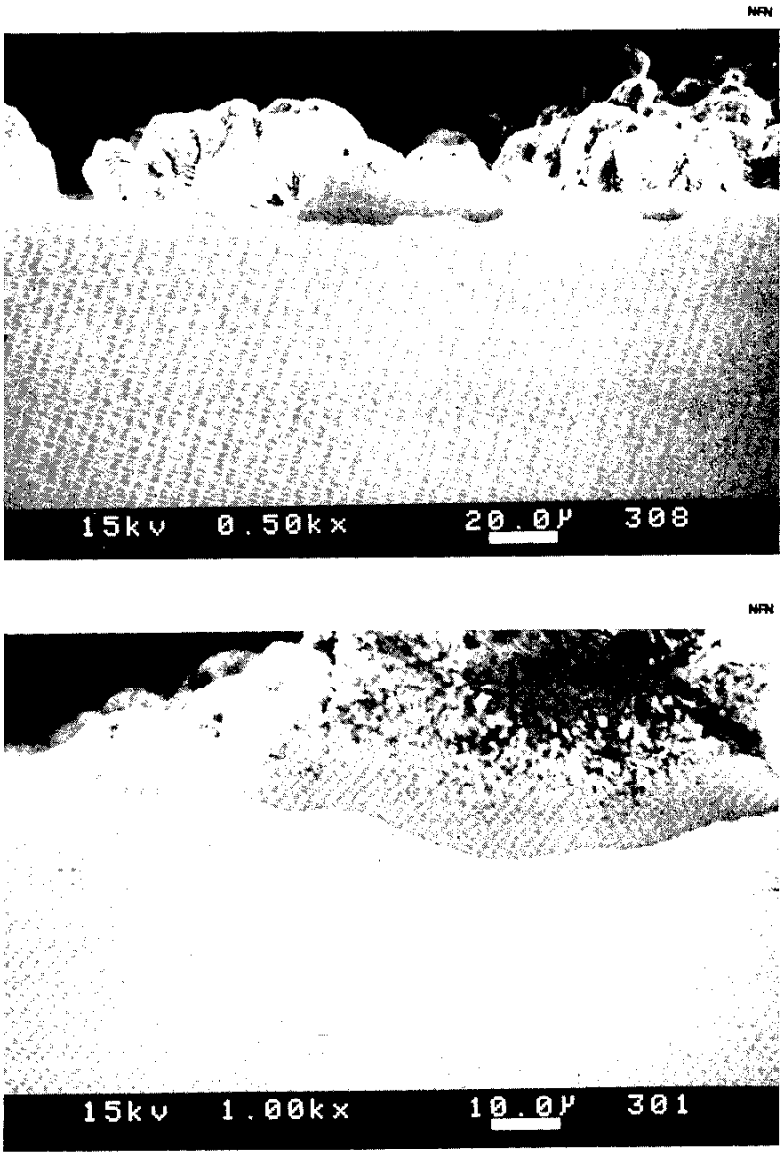

Figure 16. Scanning electron microscopy (SEM) micrographs of a cross-section of a 316L stainless steel samples exposed to molten 8001 Al alloy at 700° C.

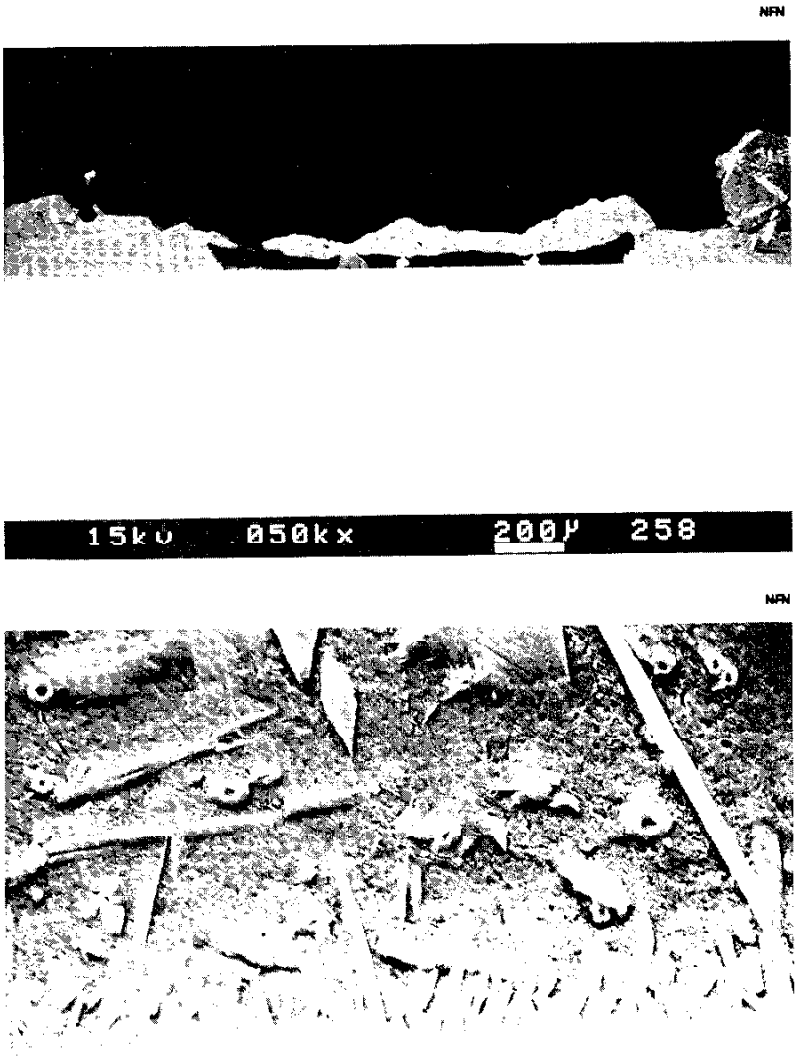

Figure 17. Scanning electron microscopy (SEM) micrographs of a cross-section of a 316L stainless steel samples exposed to molten 8001 Al alloy at 900° C.

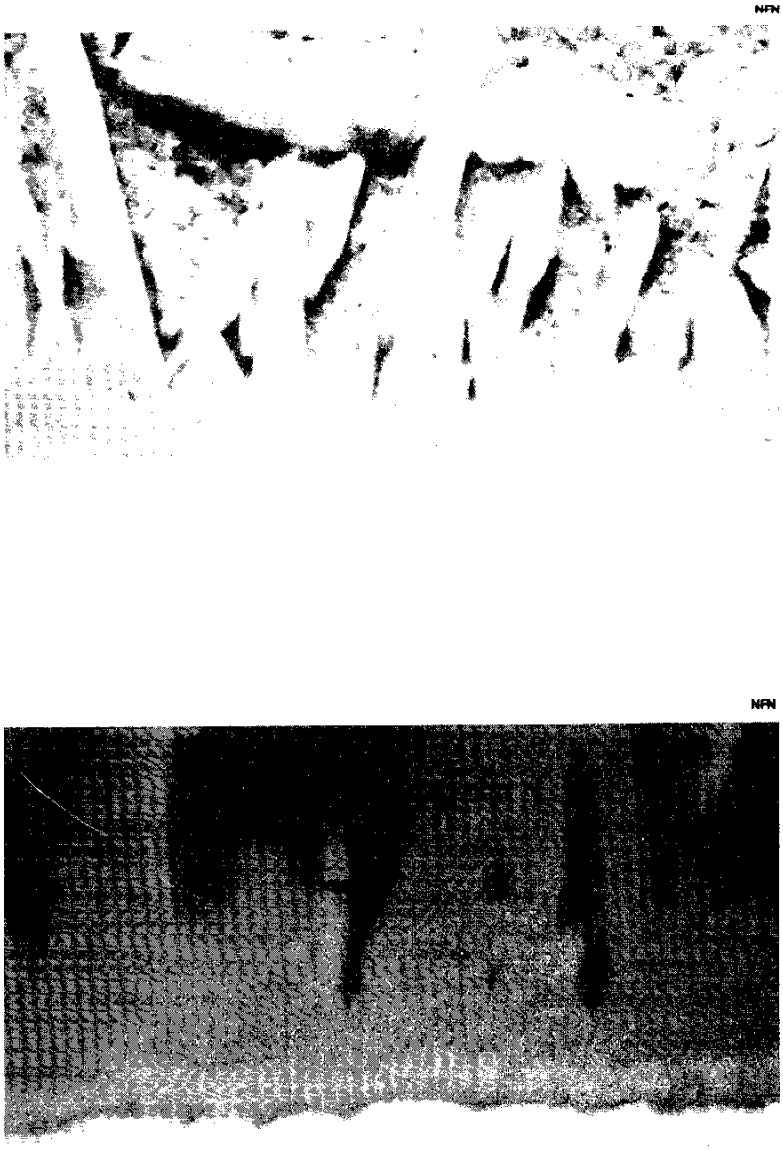

Figure 18. SEM micrographs of the interface region of a 316L stainless steel sample exposed to an 8001 Al alloy melt at 900° C. Note the two interfacial layers.

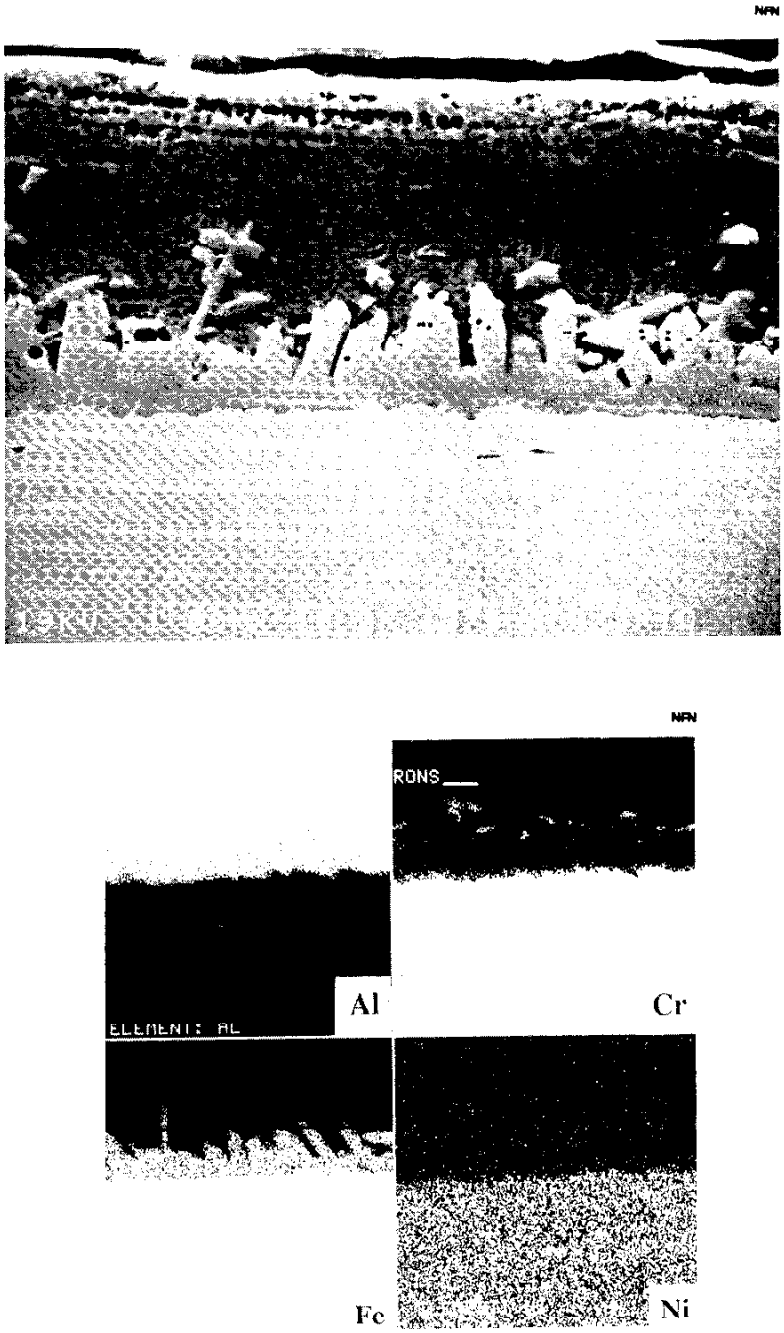

Figure 19. SEM micrograph and elemental maps of the interface region of a 316L stainless steel sample exposed to 8001 Al alloy at 900° C.

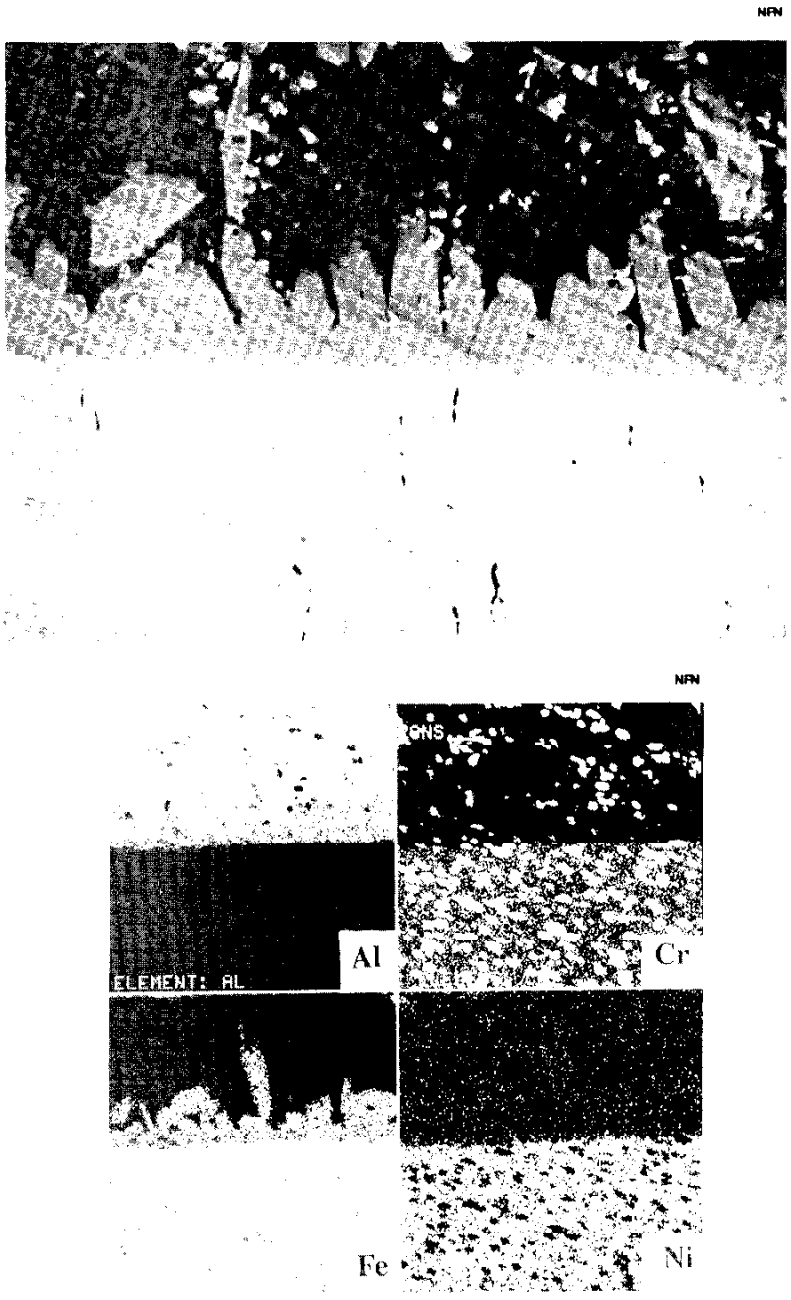

Figure 20. SEM micrograph and elemental maps of the interface region of a 304 + 1 wt % B stainless steel sample exposed to 8001 Al alloy at 900° C.

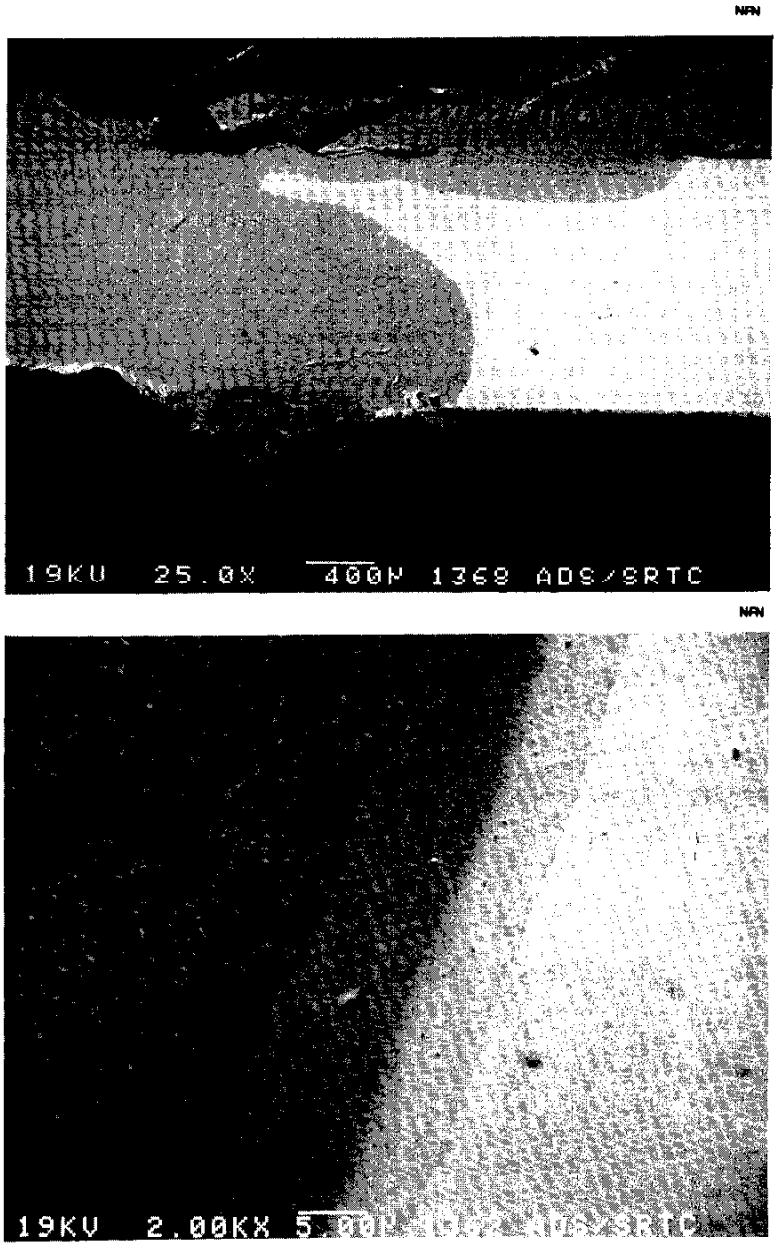

Figure 21. SEM micrographs of the interface region of a 316L stainless steel sample immersed in 8001 Al alloy for 1 minute showing attack by an apparent dual-diffusion mechanism.

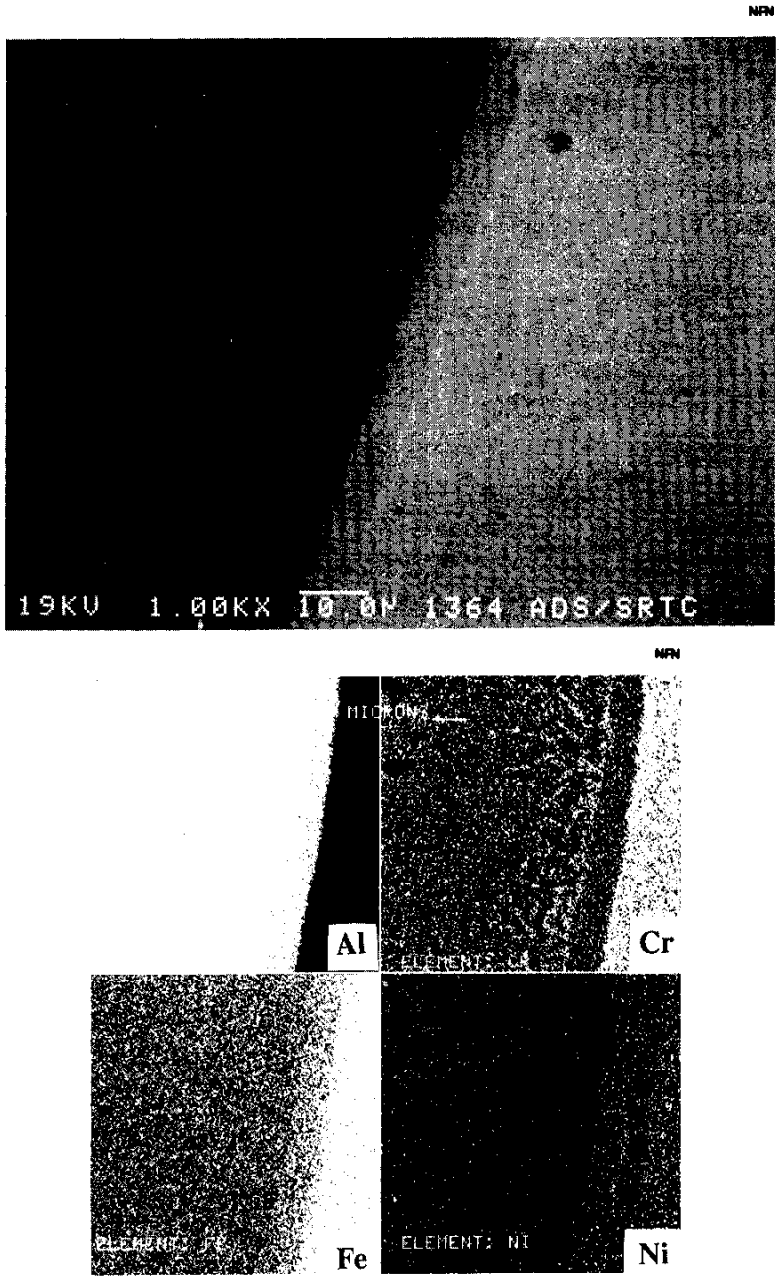

Figure 22. SEM micrograph and elemental maps of the interface region of a 316L stainless steel sample immersed in 8001 Al alloy for 1 minute.

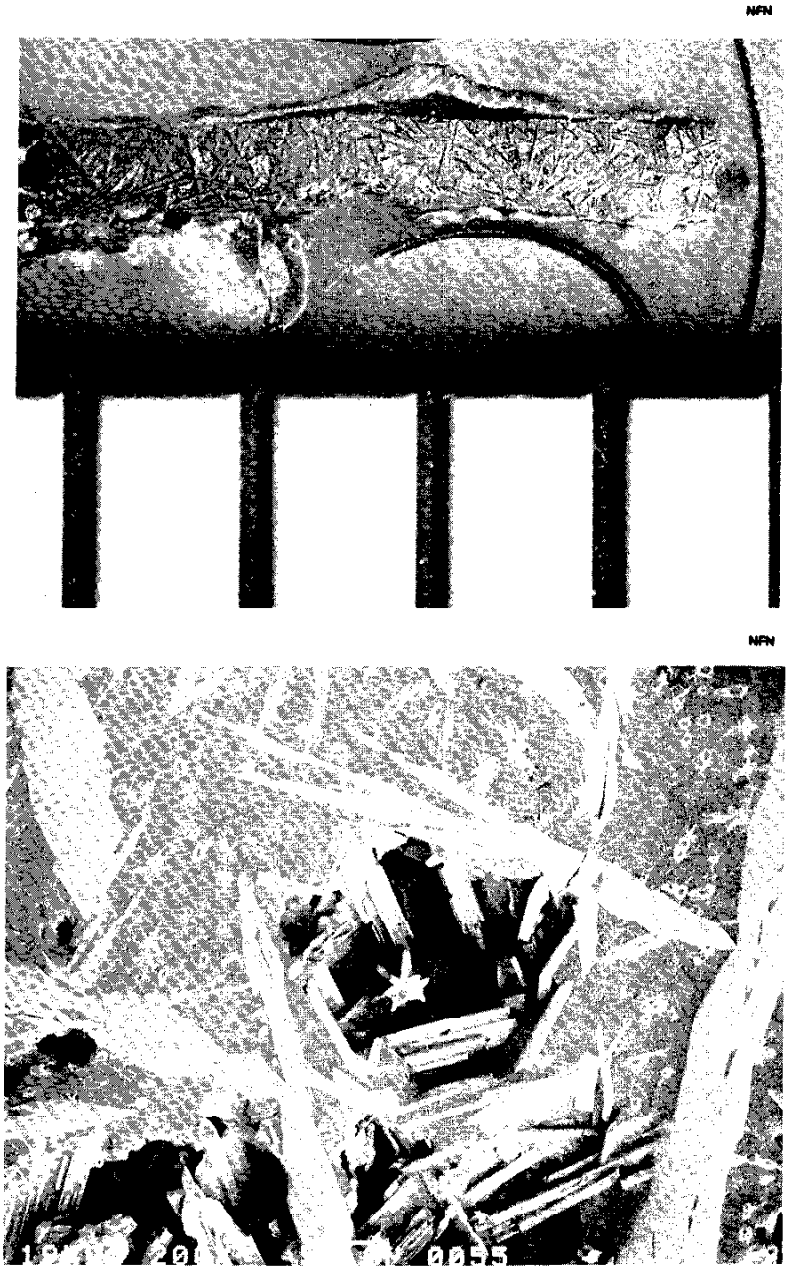

Figure 23. Micrographs of a sample completely consumed following immersion in molten 8001 Al Alloy at 1100° C for 5 minutes. Note the unique intermetallic phases formed by this interaction.

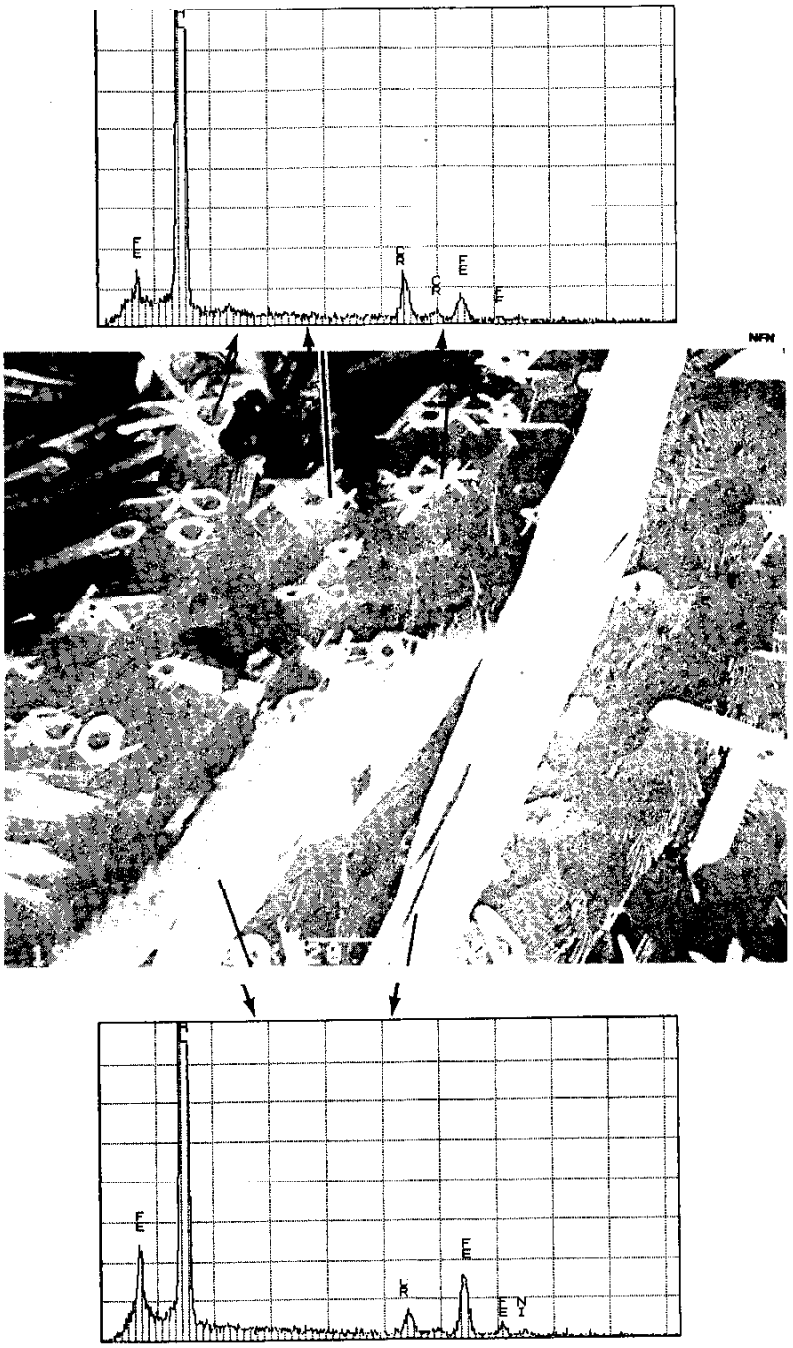

Figure 24. SEM micrographs and EDS spectra showing the two distinct phases formed by the interaction of 8001 Al alloy and 316L stainless steel at 1100° C.

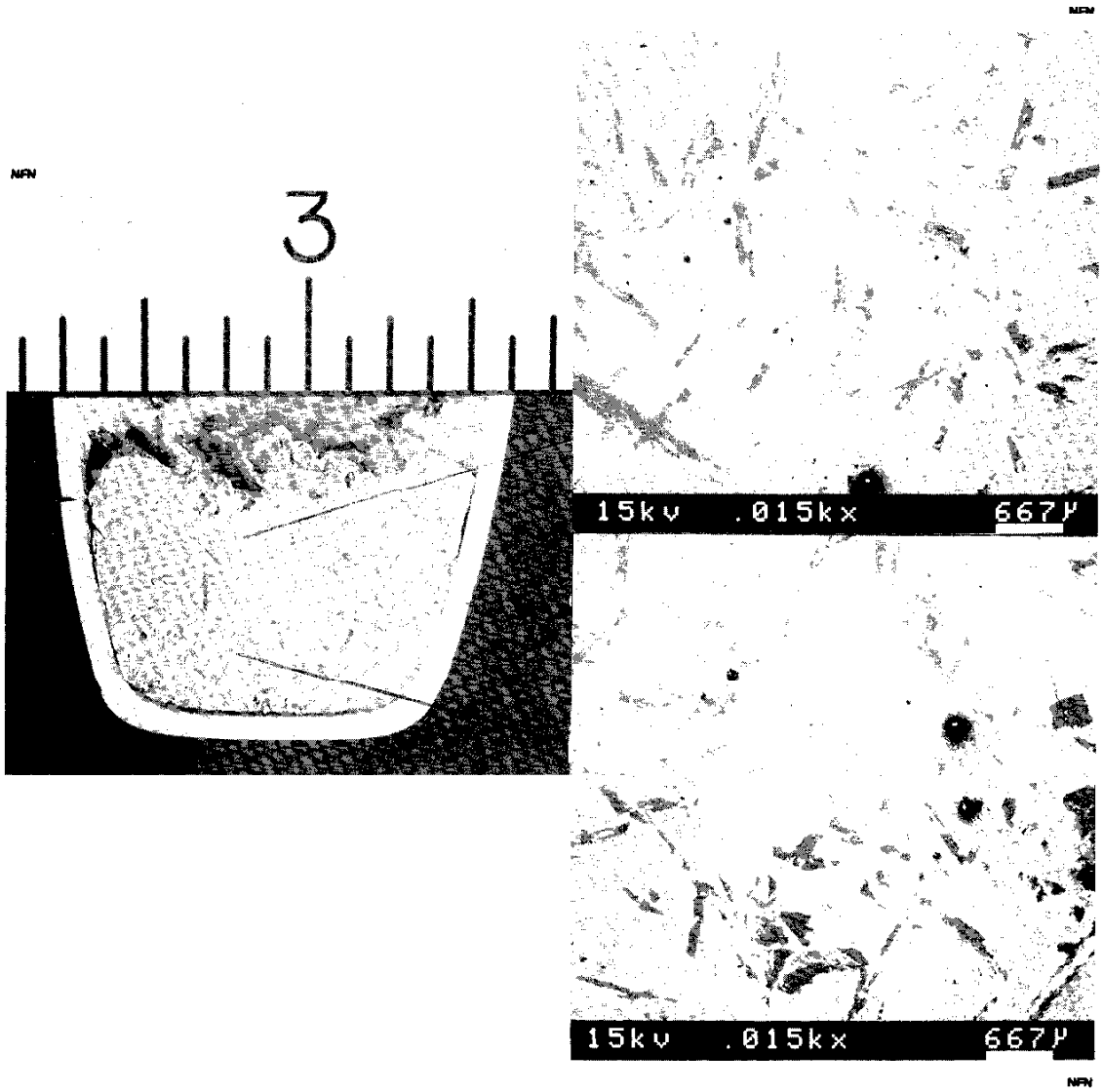

Figure 25. Micrographs of a cross-section of an 8001 Al alloy melt following immersion of 316 L stainless steel coupons at 900° C. A relative homogeneous dispersion of phases was evident at the top and bottom of the melt.

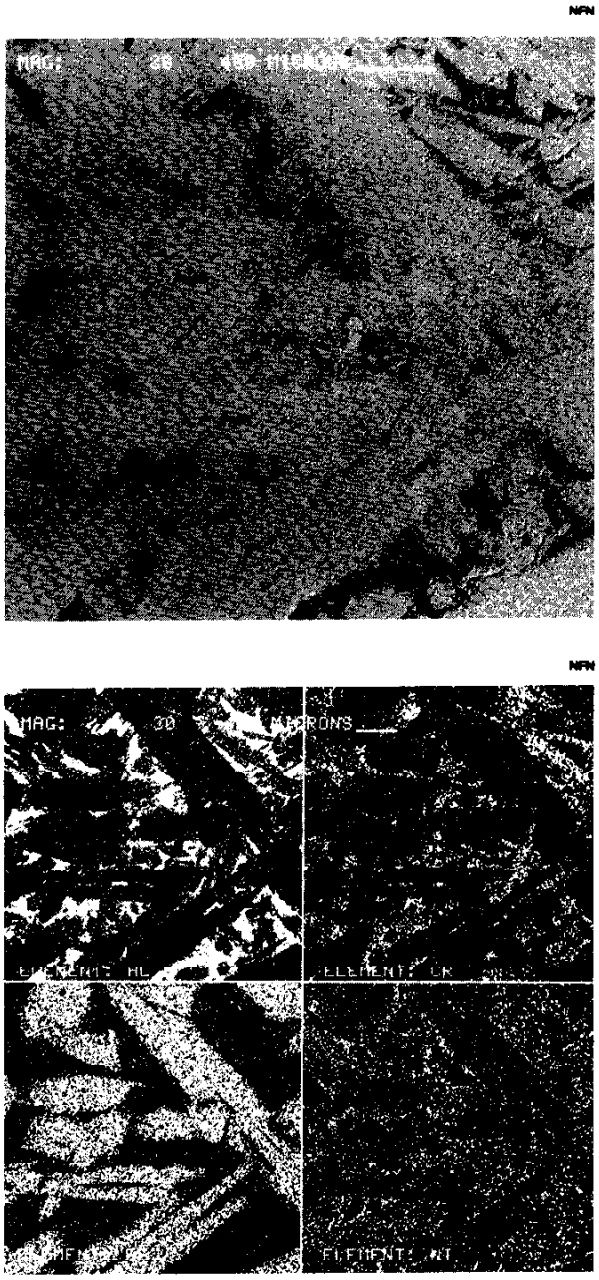

Figure 26. SEM micrograph and elemental maps of a region near the top of an 8001 Al alloy melt following immersion of 316L stainless steel coupons at 1100° C.

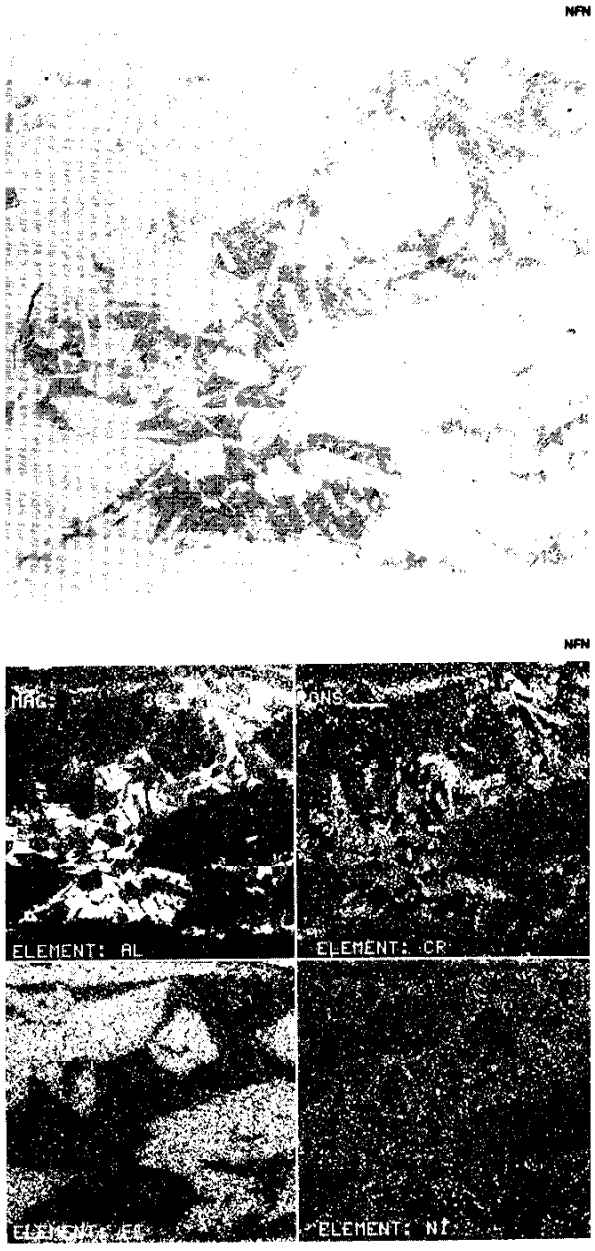

Figure 27. SEM micrograph and elemental maps of a region near the bottom of an 8001 Al alloy melt following immersion of 316L stainless steel coupons at 1100° C.

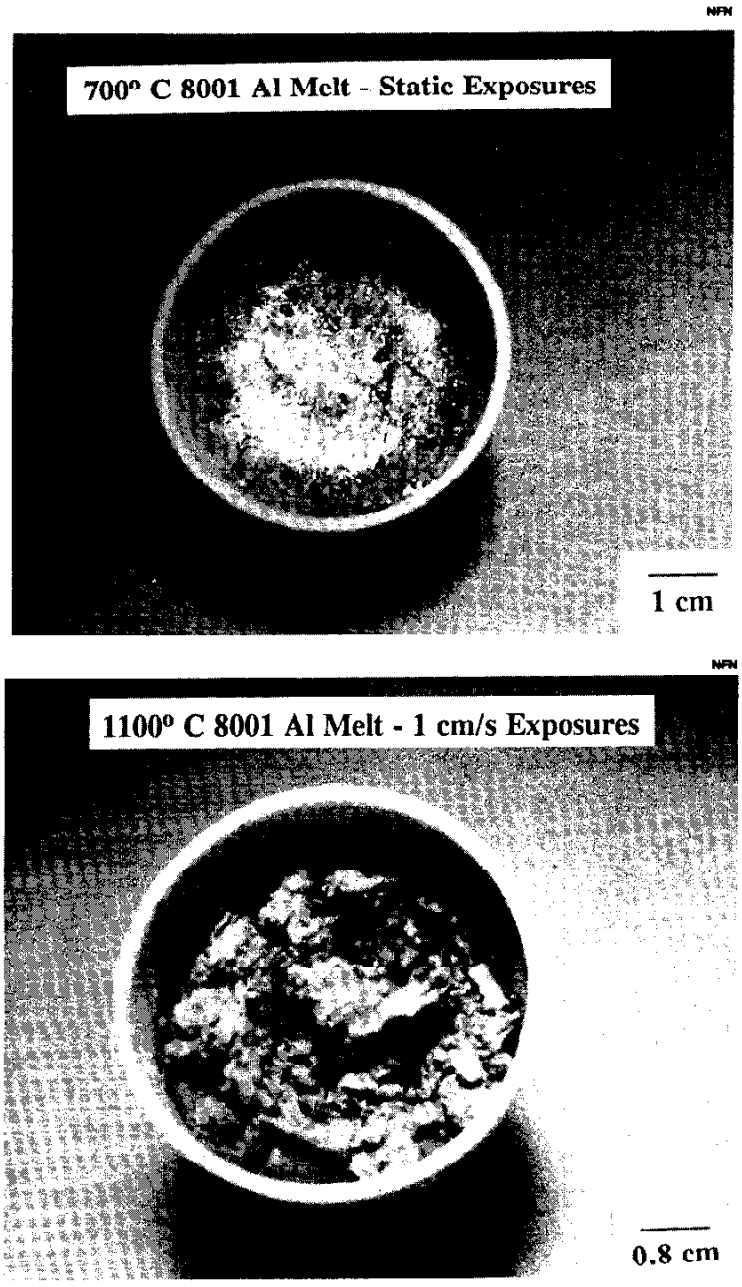

Figure 28. Photographs of 8001 Al alloy melts following contrasting stainless steel coupon exposure conditions. Note the "dross" build-up which accompanied increases in melt temperature and sample rotation.

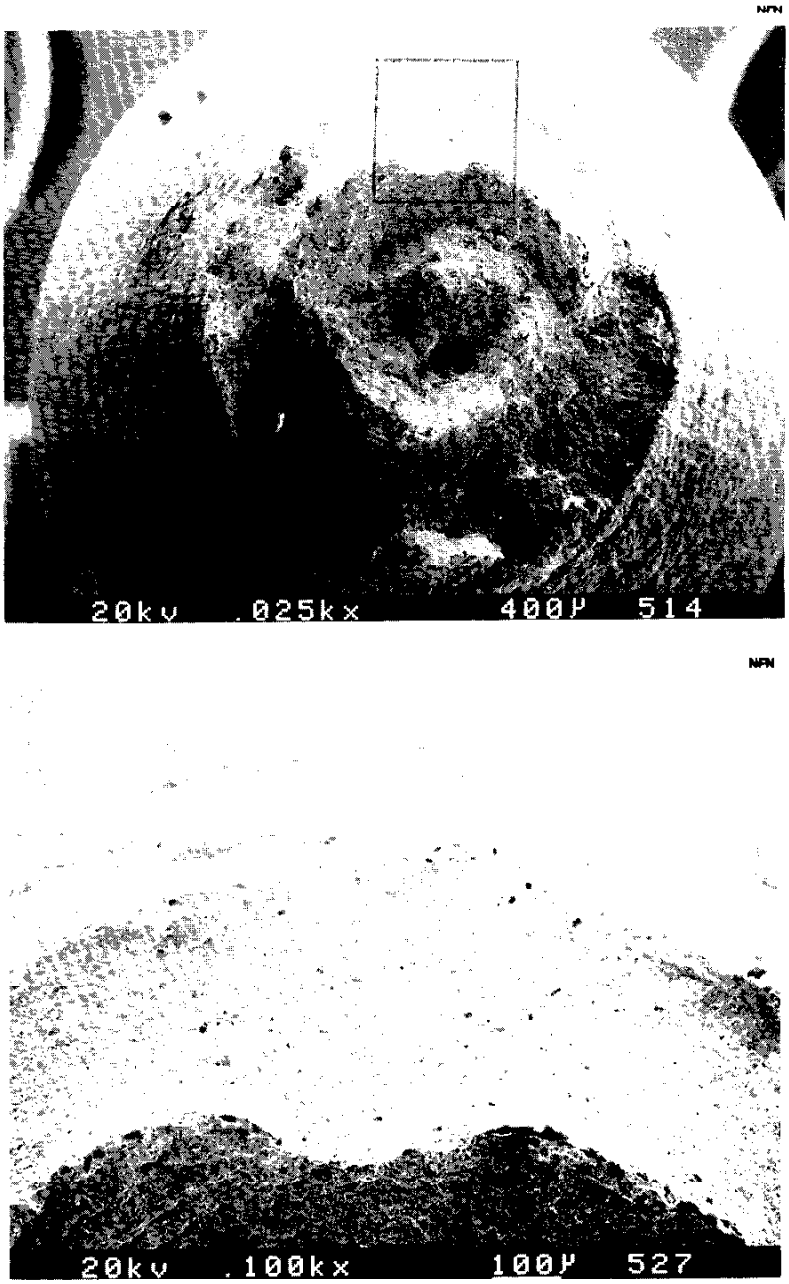

Figure 29. SEM micrograph of an uncoated 316L tensile specimen following stress-rupture testing at 750° C.

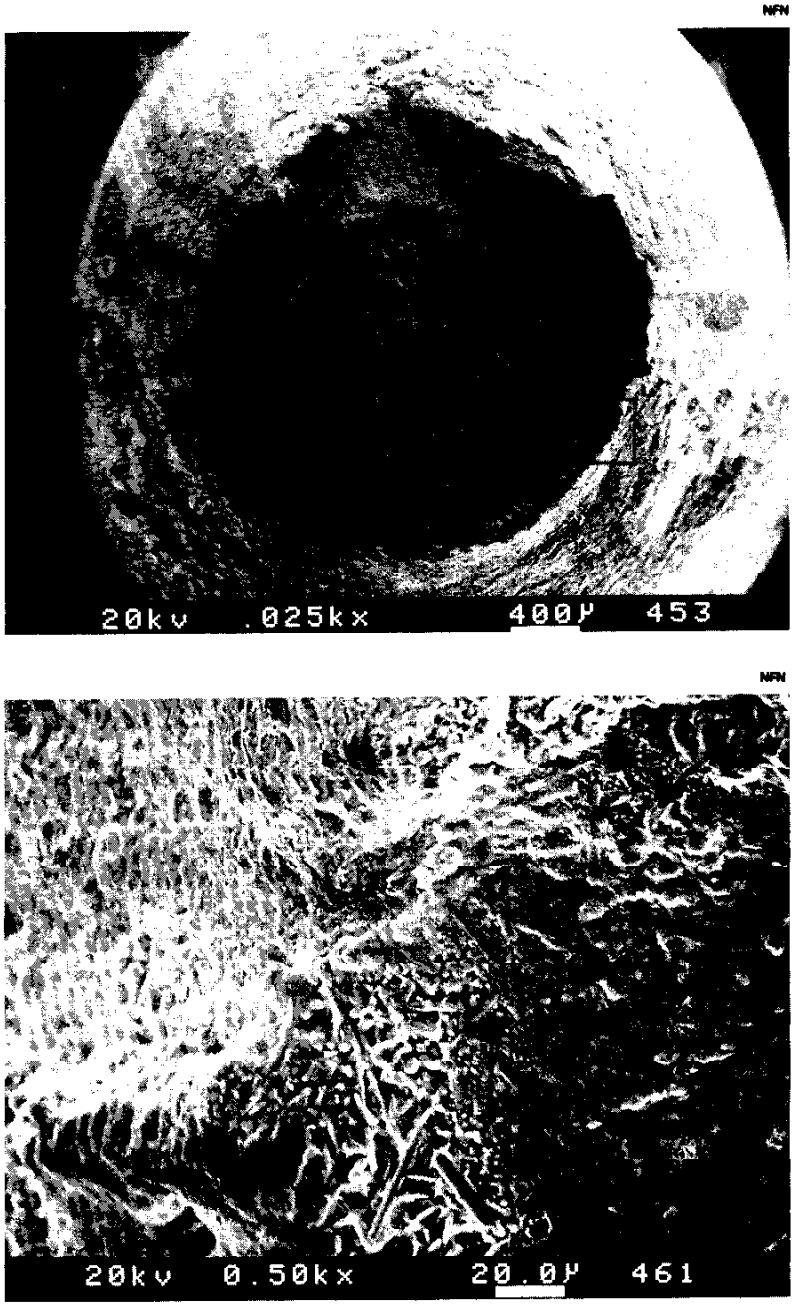

Figure 30. SEM micrograph of a 316L tensile specimen coated with 8001 Al alloy following stress-rupture testing at 750° C.

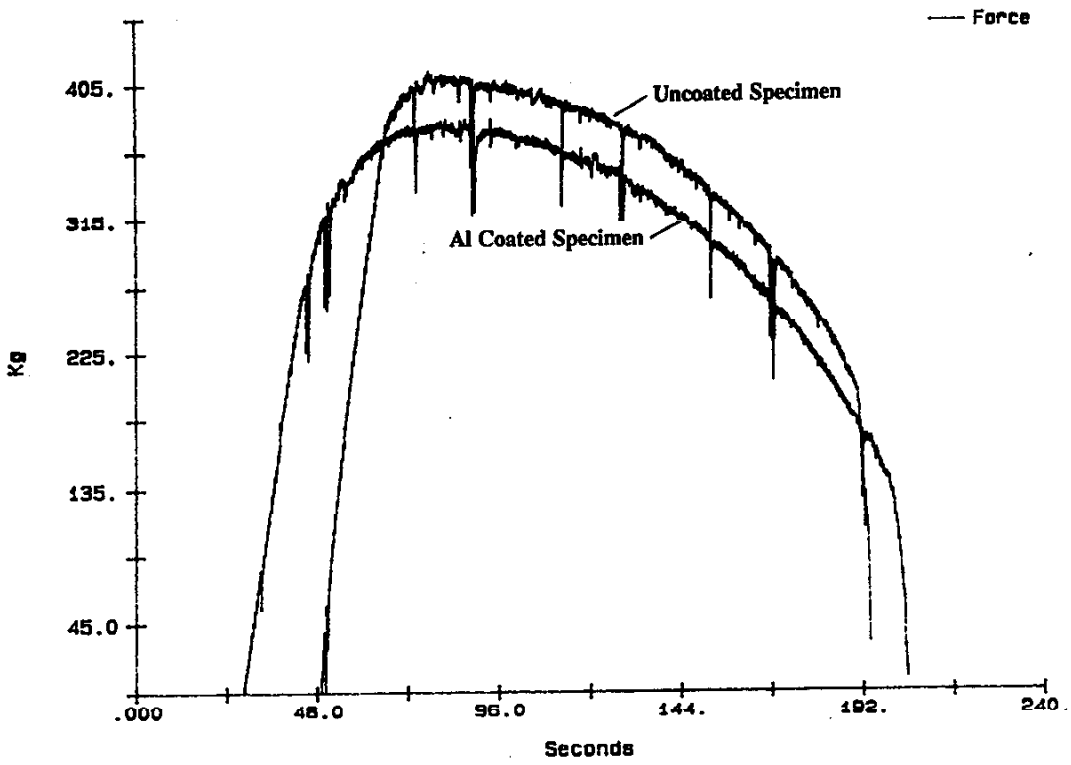

Figure 31. Plots of force vs. time for uncoated and Al coated 316L tensile specimens at 700° C for a constant displacement rate of 0.001 inch/second.

DISTRIBUTION

Westinghouse Savannah River Company

Government
Keith A. Klein, NP-30
John J. Jicha, NP-40
Robert Neuhold, NP-41
John Baker, NP-43
Amarjit Mehta, NP-44
Patrick T. Rhoads, NP-43
Robert T. Kratzke, NP-40
Jeng G. Chang, NP-43
Dionisio E. Cabrilla, NP-43
Paul W. Kaspar, NP-71
James P. Mulkey, NP-71

Non-Government
Robert C. Iotti, Ebasco
Jacek Jedruch, Ebasco
Kenneth Bergeron, SNL
Kenneth O. Reil, SNL
Scott E. Slezak, SNL
Walter Deitrich, ANL
Dae H. Cho, ANL
Bruce W. Spencer, ANL
Tom Y. C. Wei, ANL
Peter Cybulskis, BMI
Richard S. Denning, BMI
George A. Greene, BNL
James Guppy, BNL
Narinder K. Tutu, BNL
Hans K. Fauske, FAI
Michael Epstein, FAI
Jeff Martin, LANL
Crispin W. Thiessen, WSRC
Kenneth W. Cooper, WSRC
F. Joseph McCrosson, WSRC
Jerry P. Morin, WSRC
Thomas E. Britt, WSRC
M. Lee Hyder, WSRC
Peter L. Gray, WSRC
Robert T. Graulty, WSRC